INVESTIGATION OF FAULT PROPERTIES USING ELECTRICAL RESISTIVITY IMAGING

By

MATHEW E. RILEY

Bachelor of Science in Geology

Oklahoma State University

Stillwater, Oklahoma

2004

Submitted to the Faculty of the
Graduate College of the
Oklahoma State University
in partial fulfillment of
the requirements for
the Degree of
MASTER OF SCIENCE
May, 2007

INVESTIGATION OF FAULT PROPERTIES USING

ELECTRICAL RESISTIVITY IMAGING

Thesis Approved:

Dr. Todd Halihan

Thesis Adviser

Dr. James Puckette

Dr. Surinder K. Sahai

Dr. A. Gordon Emslie

Dean of the Graduate College

ACKNOWLEDGEMENTS

This research would not have been possible without the financial support of the Oklahoma Water Resources Board, the field work that was completed by students Mike Sample and Greg Federko, and equipment and software provided by the Oklahoma State University School of Geology. Support provided by the Oklahoma State University faculty was instrumental in completing this study. My advisor, Dr. Todd Halihan, deserves special thanks for finding funding for this project, providing guidance and insight, and for devoting several weekends to help me complete this work.

I would also like to express my sincerest thanks to Deborah Muncy for putting up with my stress and anxiety for the past few months so that I could complete my goals. Without her support this project would have been much more difficult to complete.

TABLE OF CONTENTS

Chapter Page

LIST OF TABLES

LIST OF FIGURES

Figure Page

Chapter I

INTRODUCTION

The Arbuckle-Simpson aquifer is a sole source aquifer comprised of fractured carbonates and sandstone in south central Oklahoma. The aquifer underlies an area of approximately 500 mi^2 in the area of the Arbuckle Mountains (Fairchild et al., 1990). The aquifer is a source of many major springs and artesian wells in the area including Vendome Well in the Chickasaw National Recreation Area. A study is currently underway to determine if the removal of additional ground water from this aquifer will affect the surrounding springs and surface water supply. To help determine the properties of this tectonically deformed and fractured aquifer, an investigation of the role that faults play in fluid flow is required.

Faults in the area were primarily mapped during the 1950's to the 1970's (Ham, 1973). These faults were mapped using aerial photography and by field study of the formations. Little is known about faults properties at depth, therefore, a cost effective method of determine the fault properties needs to be developed. The properties of the faults that need to be defined are:

1. The dip of the faults.
2. The fluid properties of the fault as a barrier or conduit to flow.

This study is part of the Arbuckle-Simpson Hydrology Study, commissioned by the Oklahoma Water Resources Board. This is a five year study to determine the aquifer

properties and determine if the sale of water from the aquifer to communities outside the basin will have a detrimental affect on the springs and drinking water supplies from the aquifer. This study is related to a study that was done previously to determine the fault properties in the area with gravity surveys, but will use electrical resistivity imaging (ERI) to investigate the faults. The data from the gravity surveys will be compared to the ERI data collected in this study.

Goals and Objectives

A combination of modeled data and field data from several sites was used in this study to determine the effectiveness of this technique in determining the properties of faults. To test if this system could define the boundaries of faults, a multi-step approach was used. First, forward modeling was done to determine the effectiveness of ERI data in determining the angle of dip of fault planes. Second, field data was collected at several field sites to show repeatability in our ability to resolve the faults. When the terrain permitted, a rotation around the fault was done to help determine the true dip of the fault. Third, ERI field data was compared with the previously collected gravity surveys.

Several objectives were met for this study; they are as follows:

1. Forward Models of Faults: The forward modeling demonstrated that faults can be resolved with sufficient accuracy. Models were tested using two ERI methods and two grid schemes. This was done because the types of data collection and processing vary for ERI data.
2. Field Data: Several electrode arrays were used across the sites. These were determined by geographic constraints such as buildings, fences, roads, and

property lines. This provided data on the influence of electrode spacing on the resolution of the fault. The amount of data collected was practical given the field constraints that were present.

3. Fault Angle: By rotating the arrays around a fault and knowing the trend of the fault, a calculation of the true dip of the fault should come to approximately the same value regardless of the orientation to the fault to the ERI data line. This was essential in determining the degree to which a fault can be resolved.
4. Data Repeatability: Completing surveys at several sites was necessary to show that the technique can be used to determine the fault angles at more than one site. Three sites were selected for this study, which included one site that was open and allowed for good survey coverage, one site that has an active spring along the fault and one site that has an exposed fault trace that allowed the comparison of the resistivity image to a measured surface fault angle.
5. Comparison with Gravity Data: Comparison of the field data with gravity data was completed to correlate with another geophysical data type. Also a comparison of measured strike and dip of an exposed fault was compared to the field data for one site. This provided a comparison with the field ERI data collected at the site.

CHAPTER II

LITERATURE REVIEW

Electrical resistivity imaging (ERI) is an indirect geophysical measuring technique that records the resistivity of an area or volume within the subsurface (Ramirez et al., 1993). Electrical resistivity methods were developed in the early 1900's, however they were not widely used until the 1970's. Recent advancements in the methods have been made with the introduction of computers to process and analyze the data (Reynolds, 1997). Additional advancements occurred with the introduction of digital switching technologies that allowed for multielectrode ERI surveys to be easily collected starting in the early 1990's.

Resistance is defined in Merriam-Webster Dictionary as "the opposition offered by a body or substance to the passage through it of a steady electric current." More precisely, the resistance (R) [ohms] is defined by Ohm's Law as:

$$R = V/I \text{ [ohms]} \quad (1)$$

V [volts] is the potential difference, or voltage drop, and *I* [amps] is the current that is passing through the material. Resistivity (ρ) [ohm-meters] is the volumetric parameter that defines resistance over a three dimensional object instead of the common one dimensional wire used in resistance experiments. Resistivity is the product of a resistance and a distance (*A/L*), where *A* [meters^2] is the area of the object and *L* [meters]

is the length of the same object. Thus we can combine Ohm's Law and the distance equation to get:

$$\rho = VA/IL \text{ [ohm-m]} \quad (2)$$

There are three common ways that electrical current may be passed through a material: electrolytic, electronic, and dielectric conduction. In earth materials, the most common type of conduction is electrolytic. This is because the fluids in the pore spaces act as conductors while the grains themselves provide little conductivity (Reynolds, 1997). For hard rock geology, changes in resistivity between rock types can be high. For example limestone can vary greatly; 100 ohm-m on the low end of the spectrum to 100,000 ohm-m on the upper end of the spectrum (Griffiths, 1993). This dramatic range is because of changes in the porosity and pore fluids throughout the rocks.

Since the electrical properties of rocks in faults should change relative to the surrounding rock units and pore fluids, ERI should be able to determine the location of the faults. Most of the problems with using ERI to examine faults were caused by a lack of data density and a lack of computing power for more complex algorithms (Demanet et al., 2001; Griffiths et al., 1993; Suzuki, et al., 2000).

The greatest advance in resistivity technology has come with the introduction of faster computers and faster instruments with data loggers. This has allowed companies such as Advanced Geosciences, Inc. (AGI) to develop switching smart electrode cables that allow automatic sampling with different arrays (AGI, 2001). Since a single survey can contain thousands of data points, these changes were necessary to make large-scale high-resolution surveys possible. Along with the advances in surveying technology the acquisition and processing techniques have advanced considerably over the past few

years. The Halihan-Fenstemaker method is one of the most advanced high-resolution ERI methods available. This proprietary method was developed at Oklahoma State University (Halihan, et al., 2005).

Resistivity Measurement of Faults

Two-dimensional multielectrode resistivity has been used since the early 1990's to help determine the location of faults. Griffiths, et al. (1993) used simple computer models to test the ability of a Wenner array to determine the location of a fault in a region of complex geology. This study noted that 25 electrodes spaced at a distance of 50 m could electrically image down to a depth of ~200 m, however it was noted that the lack of data saturation had a negative effect on the ability to image the faults in any detail (Griffiths, et al., 1993). Borehole surveys were performed that showed that faults can be imaged with good detail. With borehole surveys the fault position and displacement of the fault can be determined on the order of 1-10 m (Suzuki et al., 2000). This method does not provide enough detailed information about the structure of the faults to identify the properties such as dip. Ground penetrating radar (GPR), seismic reflection and refraction, and resistivity have all been used as an integrated investigative technique (Suzuki, et al., 2000). Resistivity has helped to provide a confirmation of the data from other geophysical techniques (Demanet et al., 2001; Cai et al., 1996). Nguyen and others (2005) used a crest line extraction process in gradient images to determine the location of a fault in the European PALEOSIS project. They used a Wenner-alpha array in modeling and data collection. Three models were compiled: a vertical fault, a dipping fault, and a step-like structure. The study identified the locations of the faults to within 1-3 meters

however no comparisons to the dipping features and the true dips of the features were made. The study noted that higher contrast ratios increased the location error (Nguyen, et al., 2005).

The primary difficulty with determining the properties of faults is the lack of data density that is required to define the location and dip of a fault at depth. Because the resolution of a survey decreases with depth, the array must be setup so that maximum data density is obtained at the site of the fault. Modeling has shown that faults are easier to image with a thin overburden less than the width of the fault zone (Louis, et al., 2002).

Resistivity Modeling

Resistivity measurements utilize four electrodes to take a single apparent resistivity measurement. When hundreds of measurements are collected with a set of electrodes, the apparent resistivity data can be inverse modeled to determine an estimate of the true resistivity at various locations in the subsurface (Ref). This modeling of resistivity data has been more common since the early 1990's with the advent of windows based resistivity software (Loke, 1996).

All numerical resistivity models rely upon a numerical grid. Most commonly, a rectangular grid is utilized. To accommodate the physics of resistivity measurements, generally, the grid consists of two horizontal grid cells located between each electrode at the surface. Vertically, the resolution of the resistivity data decreases with depth, so a grid multiplier is provided that allows for larger grids with depth. For a 56 electrode array, this provides 112 horizontal grid cells and 13 vertical cells when using a vertical multiplier of 1.1 (AGI, 2004; Figure 2.1).

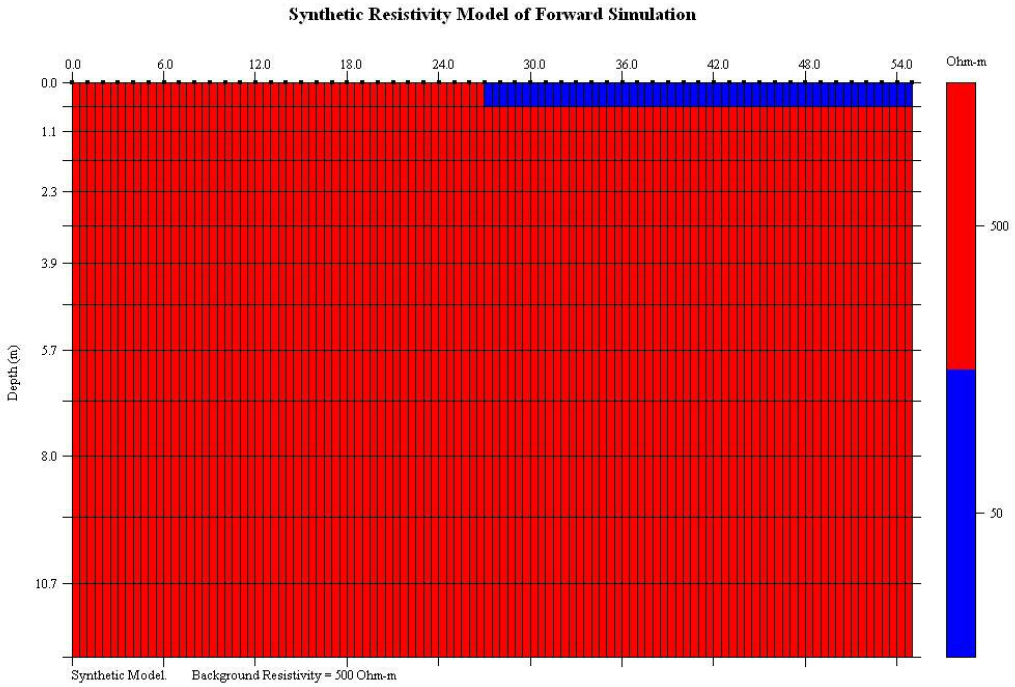

Figure 2.1. The resistivity imaging grid cell for a 56 electrode array.

The resistivity modeling software can either be used in forward or inverse mode. In inverse model mode, a set of field apparent resistivity data are provided, and the numerical grid is then used to estimate a value of true resistivity at each grid node. In forward model mode, the user inputs a set of values of true resistivity at each grid cell. The model then calculates the apparent resistivity that would be obtained given the defined grid and a specified collection array, such as a Wenner array. The model then utilizes this model set of apparent resistivity data to calculate an inverse model of the true resistivity. This study utilized both forward models to evaluate the ability to resolve dips in ERI images and inverse models to estimate dips in field ERI data.

Due to the nature of resistivity measurements the data can only be taken in a wedge shape (Figure 2.2). This is a result of the ability to resolve boundary conditions outside of this field.

Figure 2.2. Data field for a standard resistivity survey.

Gravity Data of Arbuckle Simpson Study Area

An extended gravity survey was conducted in the study area over a 20 month period in 2004 and 2005. The purpose of this gravity survey was to determine the dips of the faults in the area. Two methods of survey were conducted. A continuous gravity survey (data collected in real time as a vehicle drove the instrumentation along roads) and a standard stationary discrete gravity survey were completed (Scheirer and Scheirer, 2006). For the purpose of this study the driving survey is used.

CHAPTER III

METHODS

Two primary methods were utilized in analyzing fault structure in the Arbuckle-Simpson aquifer with ERI data. Forward models of ERI data were performed to determine the resolution of fault features available with current technology. Sources of error were identified and examined to determine the effect they have on the data and to determine how to decrease that effect.

Field data was collected to compare to the modeled data. The methods used to collect the data were described. The equipment used along with the field methods was provided.

ERI Forward Modeling

ERI forward modeling was used in this project to determine the limits of the software and algorithms for determining angular features in ERI images. The main questions that were answered determined the limits on angle resolution and the inherent errors in the grid structure. The forward models were conducted to answer the questions posed.

There are several sources of error that affect the degree of accuracy of modeled angles. The numerical grid that the modeling software uses is the source of two errors. The first error is rectangular grids will only allow a finite number of angles to be

graphically represented. The common horizontal grid cell division is one-half of the electrode spacing, meaning that there are two horizontal grid cells between each electrode. This grid structure limits the ability to resolve small differences in the angles of faults, but increasing the grid density would not provide increased information for the model.

For the ERI numerical grid several calculations were done to determine the angles that were mathematically viable. Assuming that the fault is aligned with the center of an ERI image, the angle from the surface midpoint of the ERI image to the bottom or side edges of the model grid were calculated using the following equation:

$$\tan \theta = x / z \tag{2}$$

where x [m] is the length along the line, z [m] is the depth, and θ is the angle that the modeled linear feature makes relative to horizontal. To determine the error, the difference of the result of each step along x was taken. The results of this method are shown in Figure 3.1.

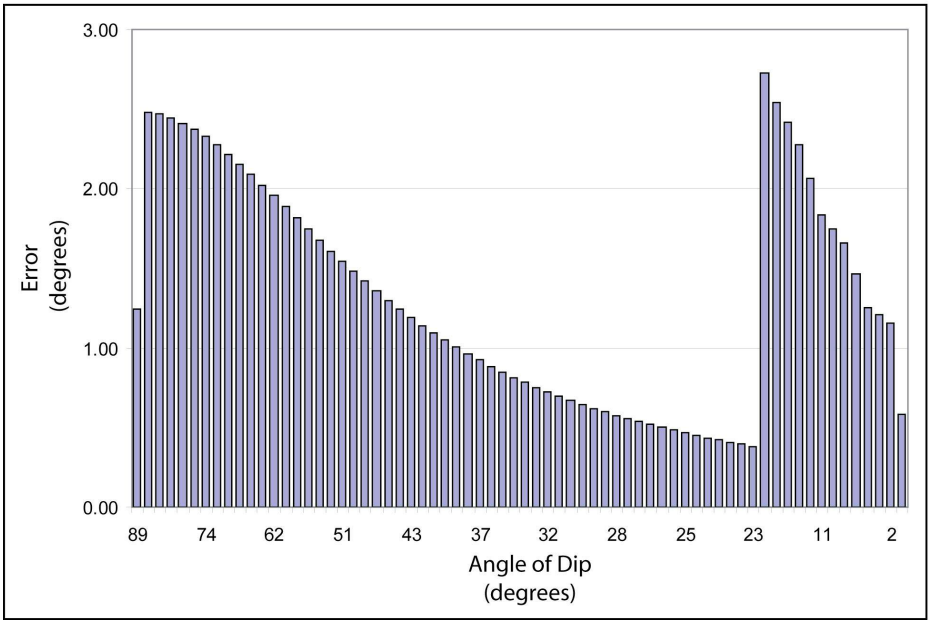

Figure 3.1. Plot of error in degrees of a linear feature from vertical (89 degrees) to horizontal (1 degree). The corner of the grid is at 23 degrees; note the increase in error at this point.

Starting at vertical the grid error is at close to a maximum of 2.5 degrees. As the angle decreases toward the corner of the model grid the grid error decreases to a point just before the corner. At this point the grid error is less than 0.5 degrees. When the angle decreases to a point around the corner of the model, in this case approximately 23 degrees, the grid error increases to nearly 2.75 degrees and then drops rapidly to a value of approximately 0.5 degrees near horizontal.

The second source of error from the numerical grid used to model ERI data was that the resolution becomes limited as the depth increases. This depth error becomes pronounced when trying to image linear features dipping at an angle of approximately 20 degrees to the grid. Figure 3.1 demonstrates this problem where at depth the thin fault crosses many grid cells on the same row.

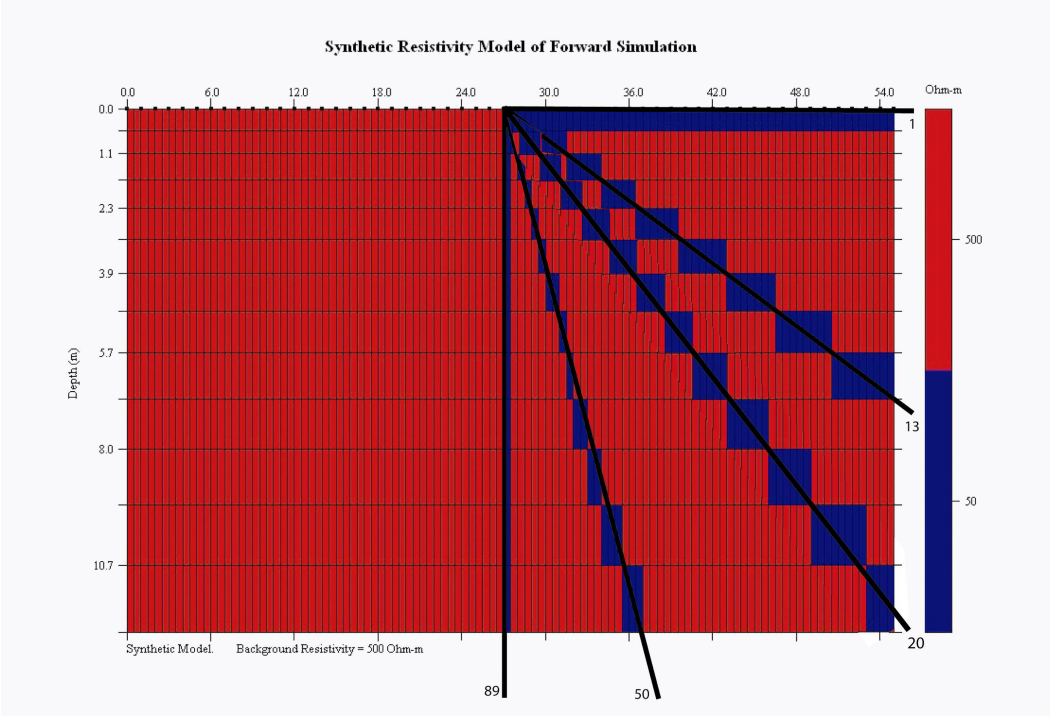

Figure 3.2. Five dipping beds and how they were modeled in this study. The five modeled angles from bottom center to upper right are: 1, 13, 20, 50, and 90 degrees.

A third source of error in the study was the acquisition errors incurred from the acquisition of the data. Polarization and contact resistance can affect the quality of the data, but measures were taken to reduce this acquisition error as much as possible. The stakes were watered with salt water, as needed, to drop the contact resistance. To reduce polarization the survey equipment uses an alternating current signal when taking measurements.

The fourth source of error is in the inversion itself. This inversion error can be large near the lower sections of the image. This is because of the skewed vertical cell length at the bottom of the model, and the inversion process. This tends to artificially increase the thickness of the fault at depth. Another error in the inversion is from the partial derivative averaging applied to the model. This error was apparent when the contrast ratios between the fault and the background increased. As the ratio increased, the blurring from the averaging spreads (Nguyen, 2005).

Forward modeling was done with the default settings in the modeling software. The parameters that were manipulated were the resistivity of the fault, the background resistivity and the angle of the fault. Since the resistivity of rock can vary, a set of model values was selected from a previous survey done at one of the sites. The average value of limestone in the area of research was approximately 500 ohm-m; this value was chosen for the background resistivity for the forward modeling.

To choose a value for the fault, field data were also used. The preliminary survey conducted on the site showed the fault was lower resistivity than the surrounding rock types. In general, faults have lower resistivity near the surface due to the breaking up of

the rocks that allows fluid to seep into otherwise non-porous rock (Suzuki, et al., 2000). From these two sources a value of 50 ohm-m was chosen for the fault.

The model run in this study was a fault with a change in resistivity only along the fault itself. There was a homogeneous resistivity provided for the media surrounding the lower resistivity fault. With this model, there were several resistivity values used to determine how much of a role contrast plays in identifying the faults. For the models, the higher resistivity values are the background and the lower values are the fault. The fault resistivity is 50 ohm-m while the background is modeled at 500 ohm-m, 250 ohm-m, 100 ohm-m, and 60 ohm-m providing contrast ratios of 0.1, 0.2, 0.5, and 0.83.

Forty-four forward models using the Halihan – Fenstemaker method were generated of a dipping fault through a homogeneous media. Table 3.1 shows the fault angles and contrasts that were modeled. The green highlighted cells indicate models that more than one method was performed on. Three groups of three angles were chosen to test the angle resolution down to 2 degrees at different critical angles. This value of 2 degrees was chosen because the grid error does not allow any finer resolution except at the 23 to 24 degree angle for a 56 electrode array with a standard grid.

Model Angle (degrees) (exact)	Grid Angle (degrees) (range)	Resistivity: Background - Fault (ohm-m) 500-50	250-50	100-50	60-50
90	89-90	X	X	X	X
86	85-87	X			X
84	81-85	X			X
74	73-75	X	X	X	X
50	49-51	X	X	X	X
31	30-31	X	X	X	X
24	23.7-24.9	X			X
23	22.9-23.7	X			X
20	18-22	X	X	X	X
13	11-15	X	X	X	X
9	8-10	X	X	X	X
3	2-4	X			X
2	2	X			X
1	1	X	X	X	X

Table 3.1. Table of all forward models done with a fault cutting a homogeneous media. Yellow highlighting indicates models were only completed with the Halihan – Fenstemaker method. Green highlighting indicates completion of models at least one of the separate methods.

Figure 3.1 showed the forward models for five of the fault angles. The five modeled angles from bottom center to upper right are: 1, 13, 20, 50, and 90 degrees. For a linear trend to pass through each of the fault dips the width of the fault must increase due to the increased vertical aspect ratio of the cells. This was most pronounced near the lower portion of the image. To help alleviate problems that occur from this effect, the last three depths on the inverted image were left out of the angle calculation.

ERI Field Methods

In the past, studies have been limited to evenly spaced electrodes dues to a lack of software that can compute complex geometries. With newer software provided by companies such as AGI, various electrode spacings can be utilized. This means that in an area where higher resolution is desired, or obstacles need to be navigated around, electrode spacings can be changed to accommodate the terrain. This advance allowed for electrode lines to be setup as close to property boundaries as possible to allow for maximum depth penetration. The effective depth that a survey could resolve to was approximately 1/5 of the total line length. The resolution of objects that can be imaged was approximately 1/2 of the minimum electrode spacing. This means that a compromise between horizontal resolution and depth must be found when there were a constant number of electrodes.

The AGI SuperSting R8 resistivity meter was used for all surveys. This meter runs up to 8 channels on each survey to increase the amount of data collected while shortening the amount of time required. AGI electrode cables were used for all data collection as well. There are two types of cables that AGI uses, smart and dumb electrode cables. The smart electrode cables have a build in switch in each electrode that allows the meter to address each electrode directly and give it instructions. The dumb electrodes require the use of a switch box to control each electrode. Both types of cables were used in this study.

Topographic corrections are necessary to adjust for the change in distance between the electrodes from the topography. If this adjustment was not made then the geometry of the electrodes would be incorrect. A laser level was used for correcting

elevations on all surveys. The laser level was a TOPCON laser with an accuracy of 1/16 inch at 100 feet. GPS data of the endpoints on each line were collected. The GPS was a contractor grade Thales MobileMapper CE. The GPS data was not collected as differential data and was only accurate to a distance of approximately ±3 meters at the end points of the lines.

Since the focus of this study was to determine fault angles as deeply as possible in the bedrock, it was determined that the maximum electrode spacing possible was required for maximum depth imaging. The following protocol was followed for survey setup:

1. The field site was visually examined to determine the locations of any major faults on the property, possible obstructions to survey line locations, and the size of the site for an idea on how long the electrode lines could be set up.
2. After locating the fault, a survey was set up perpendicular to the fault trend. This survey was setup to be as long as possible to image as deep as possible.
3. The following survey patterns were used; parallel, 30 degrees, and 60 degrees to the fault. This arrangement was designed to observe variations in the dip of the rocks, as the apparent dip should change.

Electrode Installation methods

Installation of the electrodes followed this procedure:

1. Lay out line – Measuring tapes were placed along the ground in a straight line over the terrain. Stainless steel stakes were then placed at the proper spacing locations along the entire line.

2. Insert the stakes – The stakes were then hammered into the ground if possible. At some electrode locations the stakes could not be hammered into the ground because of hard rock located near the surface. In these situations a hammer drill was used to drill a hole into the rock for the stake to be placed into. Salt water was then placed into the holes to aid in giving the stake contact to the rock.
3. Connect electrodes – The electrodes were then strung out and placed alongside the stake locations. Electrodes were attached to the stakes with a clamp, spring, or rubber band. The electrodes were connected to the resistivity meter.
4. Test contact resistance – With the electrode connected to the stake and resistivity meter, a test was completed to determine the contact resistance between the electrodes and the rocks. This served two purposes. The first is that is troubleshoots the connections and second, identifies which electrodes have a poor connection with the stake or the ground.
5. Start survey – With an acceptable contact resistance test the survey can be run. The command file is loaded into the resistivity meter and the instrument runs the survey.

Electrode Location Error

The location of the electrode lines were determined using GPS. Inherent in GPS positioning is an error of ±3 meters at the lines end members. With the longer electrode lines this error is not a major problem. This is determined from the following equation:

$$\text{Error \%} = \tan^{-1}(d / 6 \text{ meters}) \quad (4)$$

where d [meters] is ½ the line length.

Two acquisition and processing techniques were used for collection and processing of data in this study. The first imaging method used was the Halihan-Fenstemaker version 2.0. The study also utilized the latest iteration of the Halihan-Fenstemaker method, version 4.0. This method was designed for images that have the highest signal strength and lowest inversion error (Halihan, 2005).

The survey layouts were designed to provide the greatest depth penetration along with high enough resolution to image a fault's fractured zone. Since this zone can be large, the largest electrode spacing possible was used. The terrain was also a major consideration in the electrode line layouts.

Since electrode cables were not durable enough to allow vehicles to drive over the line, roads cannot be crossed without traffic control. As a result, the study was limited to sites off of roads that presented no danger to the cables or vehicles. The other limitation was permission from the landowners to access property and limited the surveys to areas within land ownership boundaries.

The surveys also had to cross the fault toward the center of the line for the best resolution at depth. This was the most critical part in designing the surveys and choosing the sites. The key was to find property that had enough open range on both sides of the fault to allow the survey line to extend out for at least 100 meters on either side. The three sites that were chosen were open enough for each of the surveys to fit the criteria.

The final choice in site selection was that the site had to be accompanied by data from gravity surveys that were done on the area in the previous year. This was necessary so that a qualitative comparison between the resistivity and the gravity data could be carried out. This limited data acquisition to the Arbuckle-Simpson study area.

CHAPTER IV

SITE DESCRIPTION

The Arbuckle- Simpson aquifer underlies an area of approximately 500 mi^2 in the Arbuckle Mountains physiographic province of south-central Oklahoma. The term "mountain" is misleading, because the topography of the area consists of gently rolling hills separated from plains by the Washita River. The river follows part of the Washita Valley fault zone. The topography reflects the degree of structural deformation of the rocks. The western part of the mountains, referred to as the Arbuckle Hills, is characterized by a series of northwest-trending ridges formed on resistant rocks that are intensely folded and faulted. The eastern part of the mountains, referred to as the Arbuckle Plains, is characterized by a gently rolling topography formed on relatively flat-lying, intensely faulted limestone beds. Neither the eastern nor the western part of the area has well-developed karst topography, but a few small karst features have developed in the western part of the area as a result of solution of the carbonate rocks (Fairchild et al., 1990).

Three field sites were selected to test ERI imaging of fault properties. The Hartman Ranch and Clement Springs site were on the mildly deformed Hunton Anticline. The I-35 Mile Marker 49 site was located in the highly deformed Arbuckle Anticline.

Eleven surveys were run in this study to determine fault properties (Table 4.1). The Hartman Ranch site had the highest concentration of surveys with eight of the eleven. Five of the surveys were run along one trend acute to the fault, where the other three surveys were at angles perpendicular, 60 degrees, and approximately 10 degrees to the trend of the fault. The Clement Springs site had two surveys. The first was perpendicular to the fault surface and the second at an angle of 60 degrees to the fault. The I-35 site consisted of one survey that was along the outcrop surface.

ERI Line Name	Starting Electrode Location (m)	Total Number Of Electrodes	Electrode Spacing (m)	Total Line Length (m)
Hartman 1	0	36	9	315
Hartman 3	279	36	9	315
Hartman 2	210	36	3	105
Hartman 4	282	36	3	105
Hartman 5	372	36	3	105
DH01Perp	0	54	E 1-28 @ 10 E 101-118 @ 9 E 119-136 @ 5	526
DH02N30W	0	54	E 1-28 @10 E 101-136 @ 9	594
DH03Para	0	36	5	175
CMT01	0	56	10	550
CMT02	0	56	4	220
I3501	0	56	2.5	137.5

Table 4.1. ERI data collected at three locations over the Arbuckle-Simpson aquifer.

Hartman Ranch

The Hartman "Mill Creek Fault" site was located ~ 1.5 miles NW of Mill Creek, Oklahoma, SE of the corner of Colvert (E1790 Rd.) and Frisco (N3460 Rd.) Roads. The legal location is NW ¼, Section 1, Township 2S, Range 4E of the Indian Meridian. The northern boundary of the site was parallel to and coincident with the end of Colvert Rd.

The GPS (NAD 27) coordinates for the northern boundary of the site, at a point 77.8 m (255 ft) east of Frisco Rd., were N34°25' 09.2", W96° 50' 40.7". These coordinates also marked the northern end of the surface ERI line on this site. The terrain on the site was gently rolling at the north end. The upper part of a hill was in the north-west corner of the site with slopes to the east and south of this corner. The hill peaked just to the NW corner of the property. A sinkhole was identified approximately 60 feet south of the northern boundary and approximately 160 feet east of the survey line Hartman 1. The surface expression of the sinkhole was a 16 ft diameter depression that is approximately 15 ft deep. The sinkhole was steep sided and free of standing water although moisture was present at the bottom, which supported the growth of moss. The site was free of any significant obstructions other than two small groves of trees. The fence along the western edge of the site was wire with wood posts that were not expected to present any 3-D effects in our ERI images. There was also a recently constructed power line that abuts the western edge of the site; however it was not anticipated to cause any problems. The site was used as grazing range for cattle by the landowner. The Kindblade Group outcropped on the north side of the fault while the Deese group outcropped on the south side of the fault.

The line perpendicular to the fault (DH01Perp) started in a small valley and went uphill as it traversed to the south-west. The terrain slowly rose until it reached a total height of about 6 meters above the valley at a point around 414 m along the line. Over this rise the terrain gradually dropped off approximately 4 meters to the end of the line at 526 meters. The south-west end of this line abutted the fence on the west side of the site. Line DH02N30W trended N30W. This line started in the NW corner of the site about 30

meters south of the north-west corner of the fence. The line started on the top of a hill and trended downhill for the entire run of the line at a rate of about .02 meters/meter or 2%. DH03Para ran parallel to the fault. There was minimal elevation change along this line.

During two separate trips to the Hartman "Mill Creek Fault" site a total of 5 surface ERI surveys along a North-South line and 3 surveys oriented at oblique angles to the fault were collected (Figure 4.1). Two of the measurements, ERI lines Hartman_1 and Hartman_3, were taken at 9.0-m (29.5 ft) electrode spacing and had an overlap of five electrodes. This configuration yielded a total of 67 electrodes along a line that acquired data over a length of 594 m (1949 ft), and a depth of 75 m (250 ft). ERI lines Hartman_2 and Hartman_4 were strung with a twelve electrode overlap and ERI lines Hartman_4 and Hartman_5 a six electrode overlap (Table 4.1). This configuration yielded a total of 90 electrodes along a line that acquired data over a length of 267 m (875 ft), and to a depth of approximately 23 m (75 ft). The 3.0-m (9.8 ft) dataset was taken near the center of the 9.0-m (29.5 ft) dataset. The sets of data were linked together by overlapping common electrodes (Table 4.1).

DH01Perp was oriented perpendicular to the fault. The first 28 electrodes were at 10.0-m spacing, 101-118 were at a 9.0-meter spacing, and 119-136 were at a 5.0-meter spacing due to space constraints of the roadway. This provided for a 54 electrode line with a total line length of 526 meters and imaging to a depth of approximately 65 m. DH02N30W was the longest line at 594 meters while still using a 54 electrode setup. Electrodes 1-28 were at a spacing of 10.0-m while 101-136 were at 9.0-m spacing. This line at 594 meters provided for an image to a depth of approximately 75 m. DH03Para

was strung parallel to the fault surface. DH03PARA used an electrode spacing of 5 m. 36 smart electrodes were the only electrodes used in this survey. The total line length for this line was 175 m, which provided image resolution down to approximately 22 m (Table 4.1).

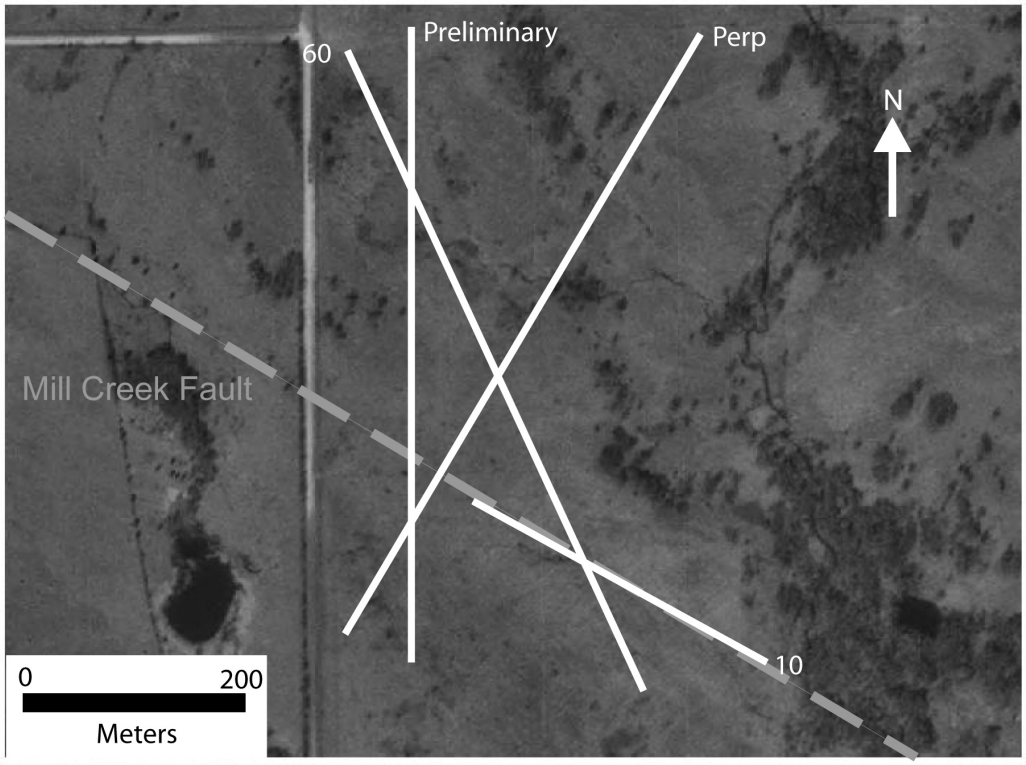

Figure 4.1. Hartman site location map with electrode line locations.

Clement Springs

The second field site in this study is Clement Spring along the South Sulphur Fault. This property is located approximately 4 miles to the north of the community of Mill Creek, Oklahoma. The property is approximately half of a section in size and is used for cattle production.

The terrain at the site is rough to the south with outcropping dolomite, that forms a small hill with a main axis trending E-W. The dolomite exposure ends about 1/5 of a mile north of the south property line. North of the dolomite exposure, the rock type changes to loose sandstone. The sandstone is weathered and forms gradual sloping hills. The southern edge of this formation is where a house is located. Just north of the house is an erosional gully, formed by a small ephemeral creek. The Clement spring is located toward the west end of the property along this creek. North of the creek bed is a gradually sloping hill that rises approximately 20 feet in elevation. This hill slopes back down to the north end of the site. Roads pass along the east and west side of the site. At the southern edge of the site is the Martin-Marietta quarry. The site is lightly forested along the creek bed and contains a large amount of poison ivy. The dolomite exposure is mostly populated by succulents, hardy grasses, and bushes. The sandstone areas are covered with prairie grasses.

Two surveys were completed at this site (Figure 4.2). The first survey was a 56 electrode survey starting at the southern edge of the site and extending to the north. The electrodes were spaced at a distance of 10 meters apart giving a total line length of 550 meters and providing resolution down to ~110 meters. The second line on the site was a 56 electrode survey starting SW of the fault and trending to the NE. An electrode spacing of 4 meters was used giving a total line length of 220 meters and providing resolution down to ~44 meters.

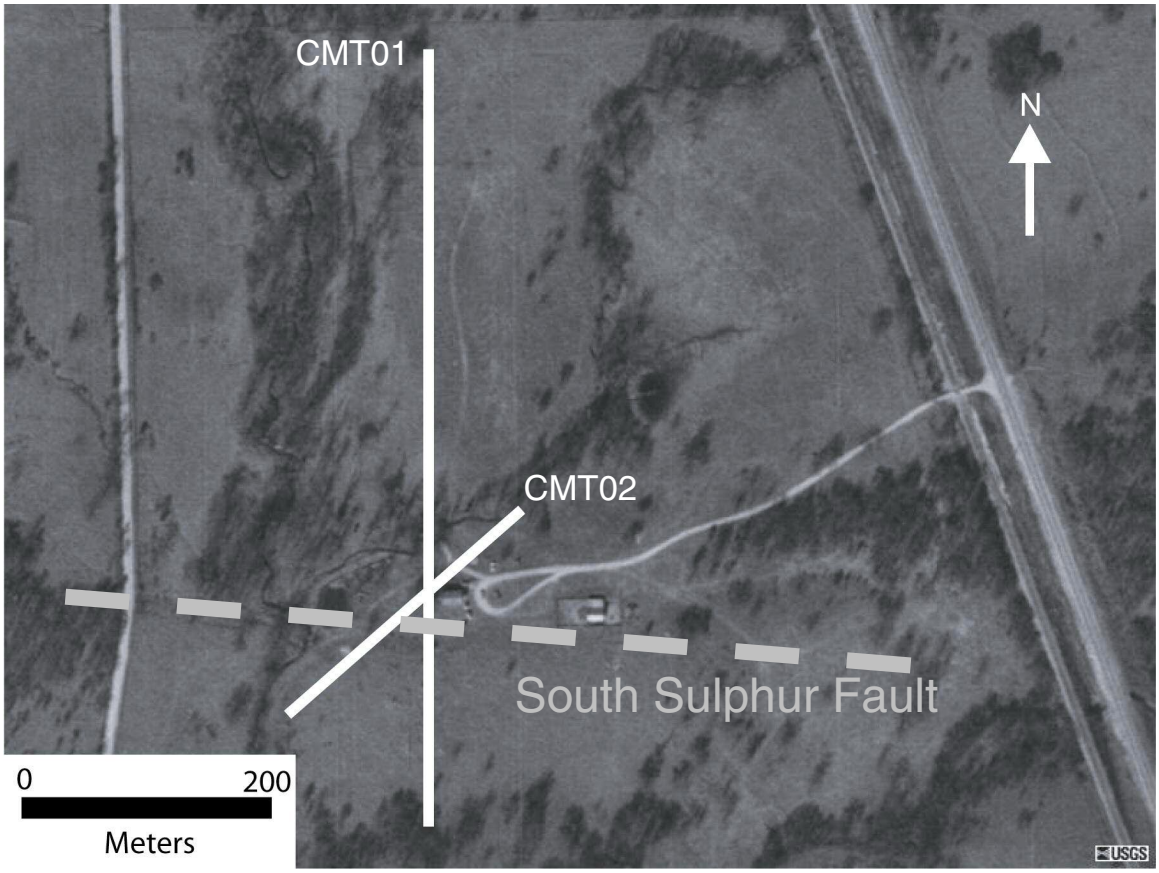

Figure 4.2. Clement Springs site location map showing electrode line locations.

I-35 Mile Marker 49

This field site is located along U.S. Interstate 35 (I-35) at the scenic turnout, mile marker 49. This turnout is a road cut for I-35 that provides a good exposure of the Collings Ranch Conglomerate (Figure 4.3). The site is on the limb of an anticline–syncline pair; however, the exposure itself is a hill. A metal post and metal mesh fence runs along the top of the hill to protect people from falling off of the exposed cliff face. The posts for this fence were set in concrete. The Vegetation along the top of the hill is composed predominantly of evergreen trees and grasses. A portion of the hill has been

paved to provide a parking area for automobiles that visitors drive. Along the base of the hill is gravel that is vegetated with grasses and a few small trees.

One line was completed at this field site. The line was oriented approximately south to north and consisted of 56 electrodes. An electrode spacing of 2.5 meters was used giving a total line length of 137.5 meters and a resolution down to ~ 27.5 meters. The main concern at this site was a metal fence, which could "short out" the survey.

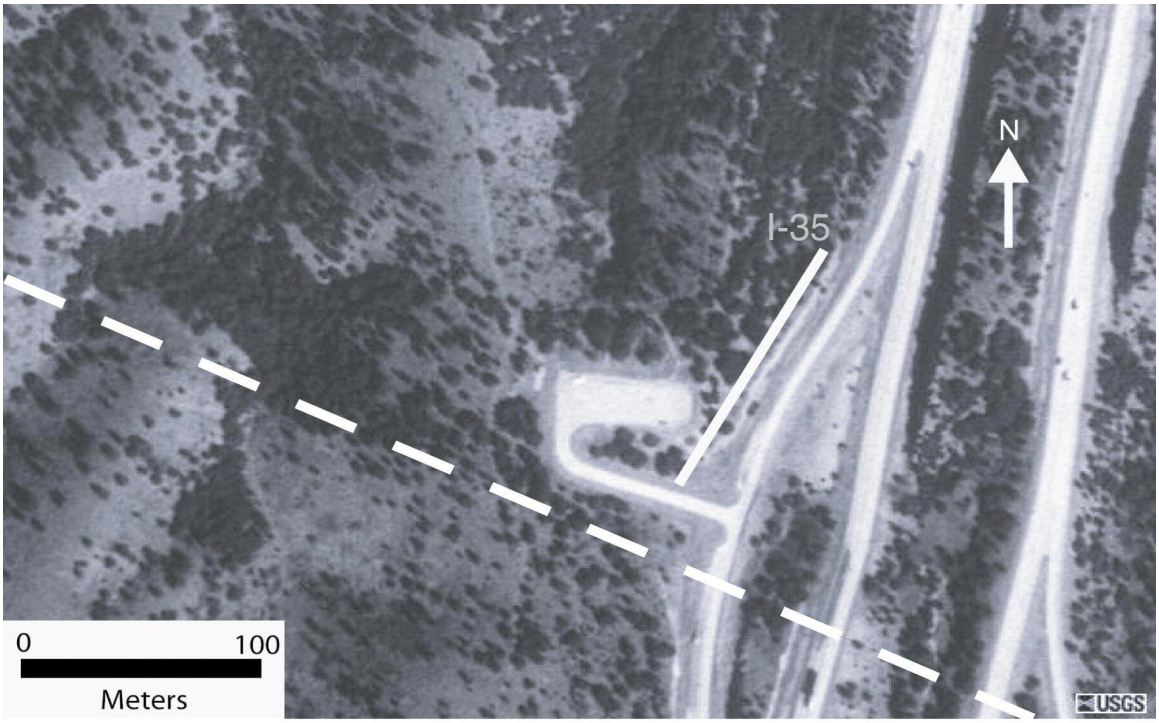

Figure 4.3. I-35 Mile Marker 49 site location showing the electrode line location.

Analysis of the dipping beds in each survey was conducted by:

1. Highlighting the zones of lower resistivity.
2. Picking the edges of these zones and calculating the angle of slope for both edges.

3. Averaging the two slopes.
4. Marking the center of the highlighted area with the average slope.

This allowed for a standardized method of picking the dipping features in the image. By picking the two edges of the zone and averaging them, the error from the inversion should be reduced. Moving the average slope to the middle of the zone is a more accurate representation for the actual location. This is supported by the modeling of the data.

CHAPTER V

RESULTS

Results for the ERI forward models are shown for contrast ratio changes and fault dips. Forty four forward models were completed using the Halihan-Fenstemaker method. Fourteen separate angles were modeled. Sixteen models were completed using a Wenner array, modeling 1, 13, 50, and 90 degree surveys. Four models each were completed for Pole-Dipole and Pole-Pole models at 1, 13, 50, and 90 degrees. For the 1, 9, 13, 20, 31, 50, 74, and 90 degree surveys all contrast ratios were modeled. The 2, 3, 23, 24, 84, and 86 degree models only the highest and lowest contrast ratios were modeled.

Field data was collected at three sites and is presented here. Four surveys were completed at the Hartman Fault site with three dipping features identified. Two surveys were completed at the Clement Springs Fault site with three dipping features identified. One survey was completed at the I-35 site; no dipping features were identified.

ERI Forward Modeling

The forward modeling was inverted and the raw data transferred to Microsoft Excel. For faults that intersected the bottom of the image, a Microsoft Excel algorithm analyzed each row of nodes from the modeled data and picked the lowest resistivity present. For models that the fault intersected the edge of the image the algorithm was

altered to examine the columns of nodes. The first one and final three data points for each calculation were dropped. The average slope of the remaining data was then taken. The result was the calculated slope of the fault that was used in this study. Table 5.1 shows the calculated slopes from the inverted models.

Angle (degrees)	Resistivity: Background – Fault (ohm-m)			
	500-50	250-50	100-50	60-50
90	90	88	88	86
86	90			87
84	90			80
74	88	84	80	77
50	78	59	54	54
31	42	42	38	38
24	36			35
23	61			29
20	29	29	29	28
13	17	17	15	17
9	11	10	11	10
3	5			3
2	3			5
1	3	3	3	3

Table 5.1. Calculated dip values for each of the forward models using the Halihan – Fenstemaker method.

All forty four Halihan – Fenstemaker models completed in this study showed similar results when the contrast ratios were changed. As the contrast ratio was increased from a multiple of 1.2 to a multiple of 10, the same changes were present across all images. The first change was that the accuracy of the pick of the fault increased with a decrease in the contrast ratio. The second change was that the fault became more difficult to identify as the contrast ratio was decreased.

Figure 5.1 shows the forward model for the 74 degree dipping fault. This fault was modeled at all four contrast ratios. Figure 5.2 shows the fault at a 500 ohm-m background and 50 ohm-m fault. The fault in this figure calculates to be 88 degrees.

Figure 5.3 shows the fault at a 250 ohm-m background and 50 ohm-m fault. The fault in this image calculated at 84 degrees. Figure 5.4 shows the same model with a contrast ratio of 100 ohm-m to 50 ohm-m. The fault in this image calculated to be 80 degrees. Figure 5.5 shows the same model with a contrast ratio of 60 ohm-m background and 50 ohm-m fault. In this image the fault calculated to be 77 degrees. This is a typical example for how the modeled images look from one extreme to the other.

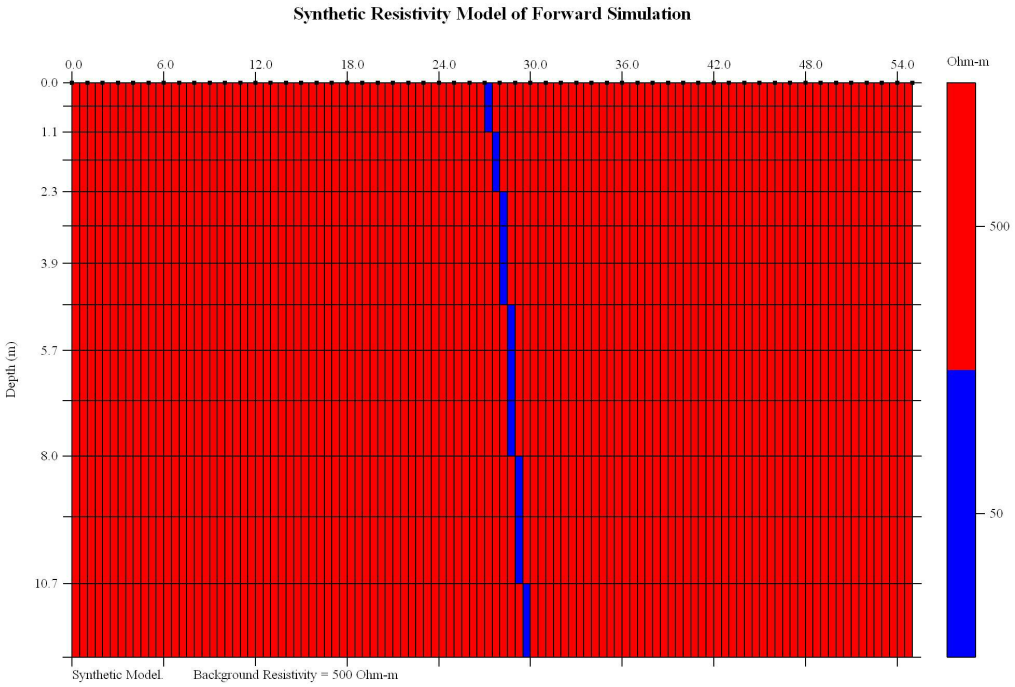

Figure 5.1. A 74 degree fault in the forward model.

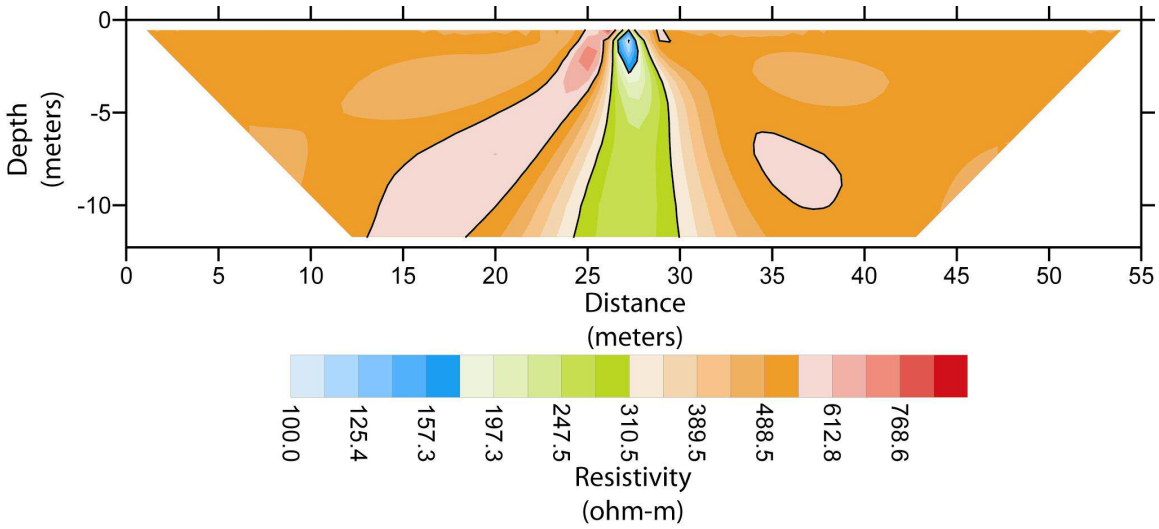

Figure 5.2. The result of the 500 ohm-m background 50 ohm-m fault forward model.

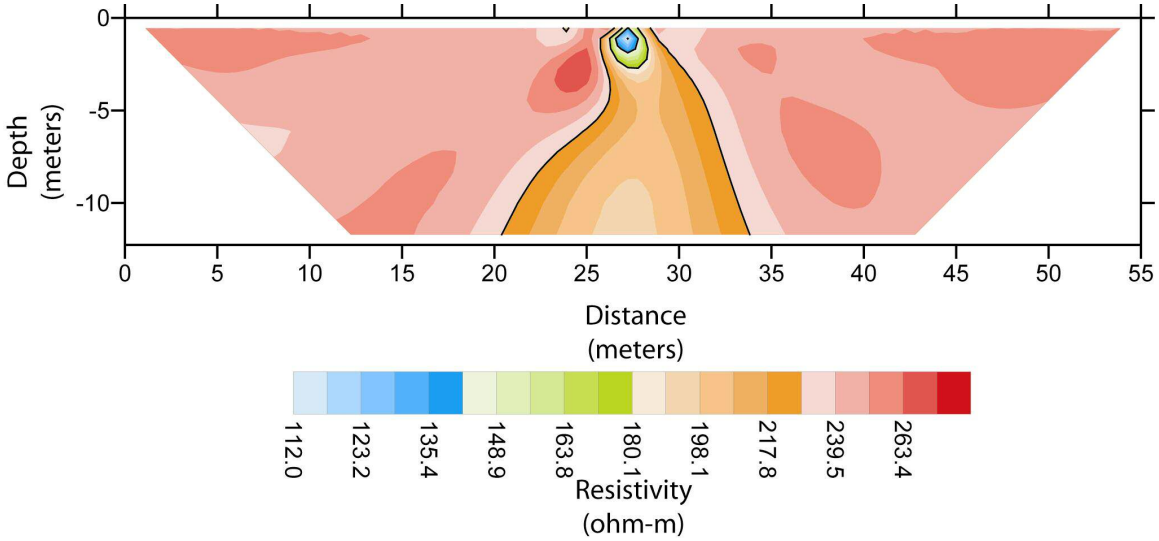

Figure 5.3. The result of the 250 ohm-m background 50 ohm-m fault forward model.

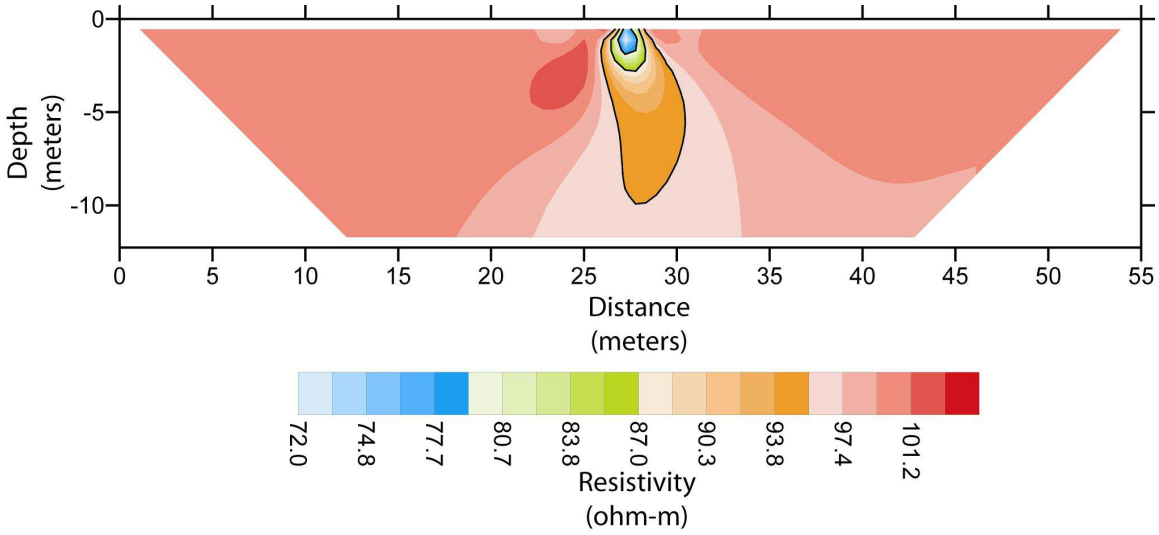

Figure 5.4. The result of the 100 ohm-m background 50 ohm-m fault forward model.

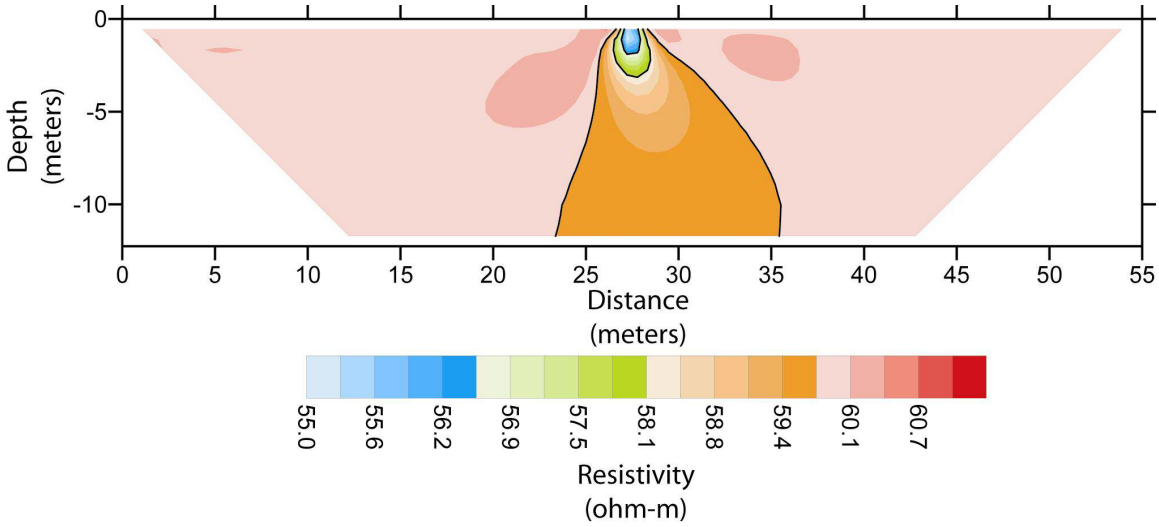

Figure 5.5. The result of the 60 ohm-m background 50 ohm-m fault forward model.

Several models were completed utilizing various techniques to compare to the Halihan-Fenstemaker method (Table 5.2). Sixteen Wenner array models were completed. The four contrast ratios were completed on 1, 13, 50, and 90 degree faults. The Wenner results suggest that the Halihan – Fenstemaker method is more consistent. However, there were a couple of occasions that the calculated Wenner dip was more accurate than the Halihan – Fenstemaker method in lower contrast situations.

Four models were completed using the Pole-Dipole method. The Pole-Dipole method was the least accurate of the four methods modeled. It consistently under predicted steeply dipping faults and over predicted shallow dipping faults. Four models of the Pole – Pole method were also completed. The Pole – Pole method was more accurate than the Wenner at 1 degree and 90 degree faults. The Pole – Pole method may have been a good alternative to the Halihan – Fenstemaker method. However, the requirement of two infinity electrodes at 10 times the electrode spacing, in this case 5 kilometers, was impractical in this study.

	Halihan - Fenstemaker				Wenner				Pole - Dipole	Pole-Pole
Angle (degrees)	Resistivity: Background - Fault (ohm-m)									
	500-50	250-50	100-50	60-50	500-50	250-50	100-50	60-50	500-50	500-50
1	3	3	3	3	87	1.2	1.2	1.2	10.2	0
13	17	17	15	17	16	16	14	14	18	8
50	78	59	54	54	75	85	45	51	73	84
90	90	88	88	86	90	132	93	88	79	90

Table 5.2. The results of the Halihan – Fenstemaker, Wenner, Pole – Dipole, and Pole – Pole forward models.

ERI Field Surveys

Several dipping features were identified in the study. The accuracy of these dipping features was determined by error calculations based on the modeling and GPS errors. At the Hartman field site four surveys were run. In those surveys two dipping features were identified. Both originated near the middle of the survey lines. Clement Springs had two surveys run at the site. Three dipping features were identified at this site. Two were on the southern end of the site while one was at the northern end. One survey was run at the I-35 site. No dipping features were identified at this site.

Hartman Site

The preliminary images for the two 9 meter surveys were combined and inverted in one file. The result of this file is figure 5.6. A low resistivity anomaly is evident in the upper part of the image from 100 feet to 400 feet and from 500 feet to 750 feet. Each is about 25 feet thick. Just below these two low resistivity anomalies there are two high resistivity anomalies. After modeling and seeing the effect that a low resistivity anomaly can cause, the high resistivity anomalies at 150 and 610 feet along the line may be abnormally high values. Also note that the zones occur only beneath the low resistivity values. At 400 feet along the line and 100 feet deep there is another low resistivity anomaly that occurs. At 850 feet along the line and 100 feet deep there is a second low resistivity anomaly. At 1200 feet there is an abrupt change in the resistivity values from the north side to the south side. This is a feature dipping at ~50 degrees to the north. On the north side of this fault are rocks of the West Spring Creek / Kindblade formations; on the south side of this zone are rocks of the Deese group. Hand samples were collected along the survey line and analyzed. The composition of these samples supports this conclusion. To the south of the fault zone in the Deese Group there is little change in the relative resistivity of the rocks.

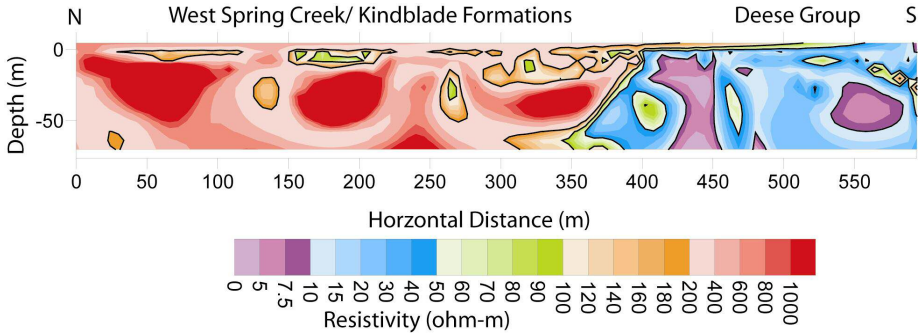

Figure 5.6. Inverted resistivity section of the preliminary survey done at the Hartman Ranch field site showing the Mill Creek Fault Zone.

Further analysis was completed on this line to identify the major dipping features. Figure 5.7 shows the low resistivity anomalies identified in the data set. In this analysis, the same dipping feature is analyzed at two different scales. The upper image with feature A is a shorter, 36 electrode, survey. Feature A in this image is dipping at 63 degrees and has a large area that was inverted as the lower resistivity zone. Note that the grid error will be larger in this image due to less grid cells relative to the total line length. Feature B is located on a longer line run along the same location. This line has the feature dipping at an angle of 102 degrees. The fault is interpreted as extending to the surface at this location along the survey line.

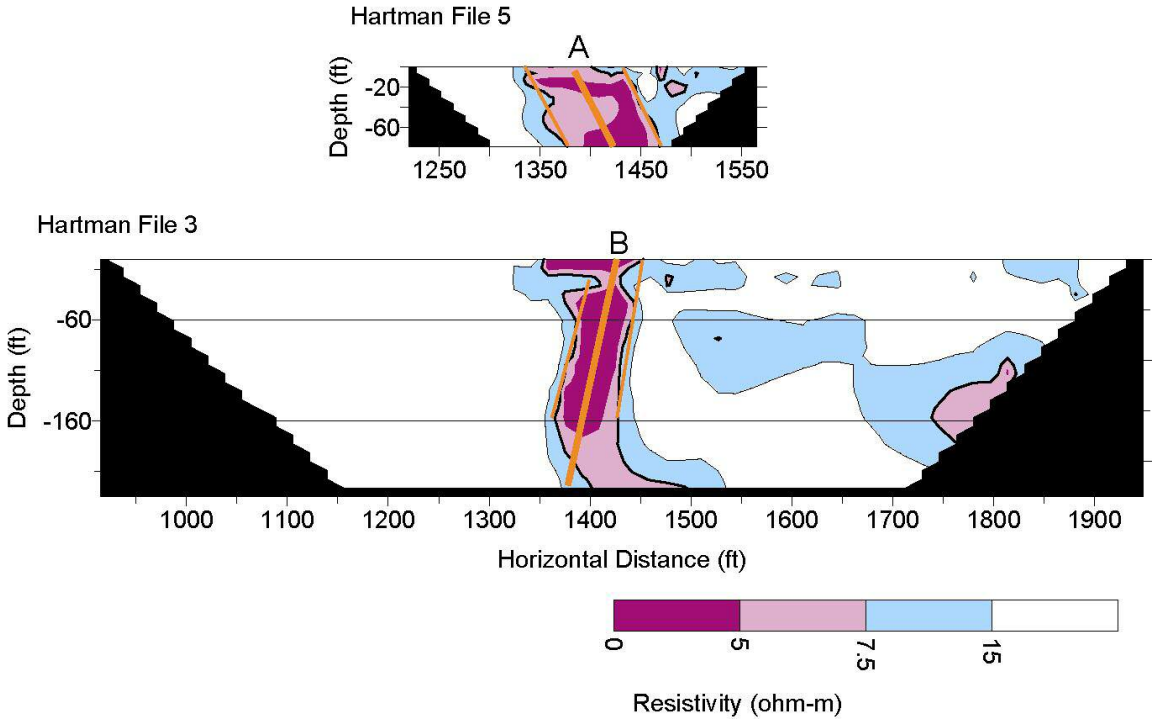

Figure 5.7. Two surveys taken at the Hartman Field site showing the same dipping feature at two separate scales. The upper image with feature A is a short line that shows the increased dispersion caused from grid error on lines with less electrodes. The lower image contains feature B that is more defined with consistent slopes on both sides of the low resistivity zone.

DH01PERP Analysis

On the northern edge of the survey near the surface from 0-100 meters is a lower resistivity signature. From 225 – 300 meters there is another low resistivity. At 340 meters along the upper edge of the survey there is a lower resistivity plane that is dipping to the north – east with an apparent dip of ~45 degrees. At 350 meters there is a near vertical feature of low resistivity. West of the vertical feature is generally higher resistivity than the east side of the feature. The west side of this feature should be rocks of the West Spring Creek/ Kindblade formations and east of the feature are rocks of the Deese Group. Most of the low resistivity trends in the Deese Group seem to have a near vertical trend, which could reflect features associated with the fault (Figure 5.8).

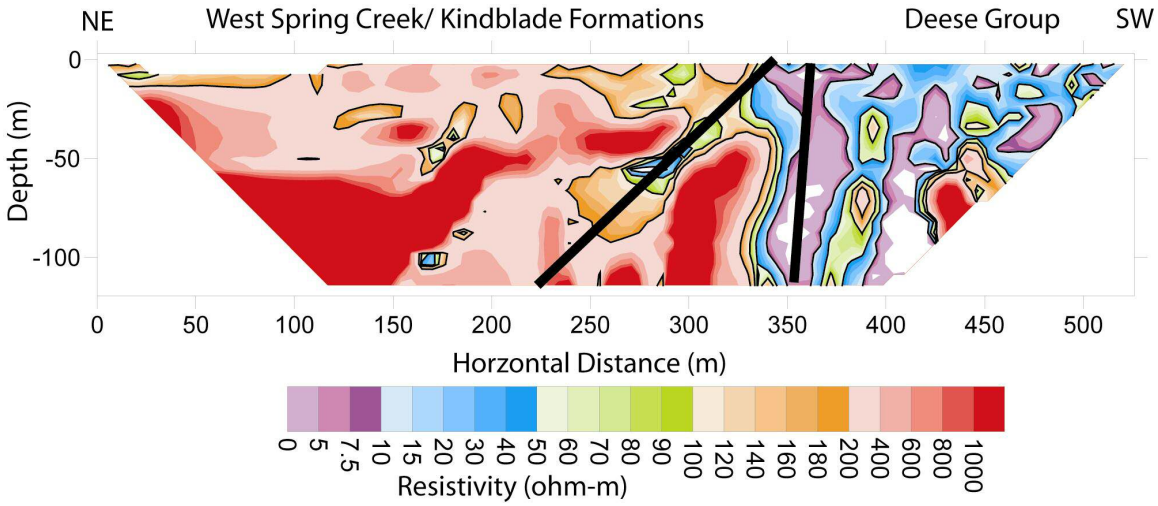

Figure 5.8. DH01PERP inverted resistivity image showing what appears to be a near vertical fault at 350 meters and a feature dipping at 32 ± 5 degrees at 325 meters.

The analysis was extended on this line to interpret the dipping features. Figure 5.9 shows three dipping features inferred from resistivity trends present in the data set. Feature A is the shallowest dipping feature interpreted in the low resistivity zone. Feature B is dipping at an angle of 96 degrees. Feature C is dipping at 108 degrees.

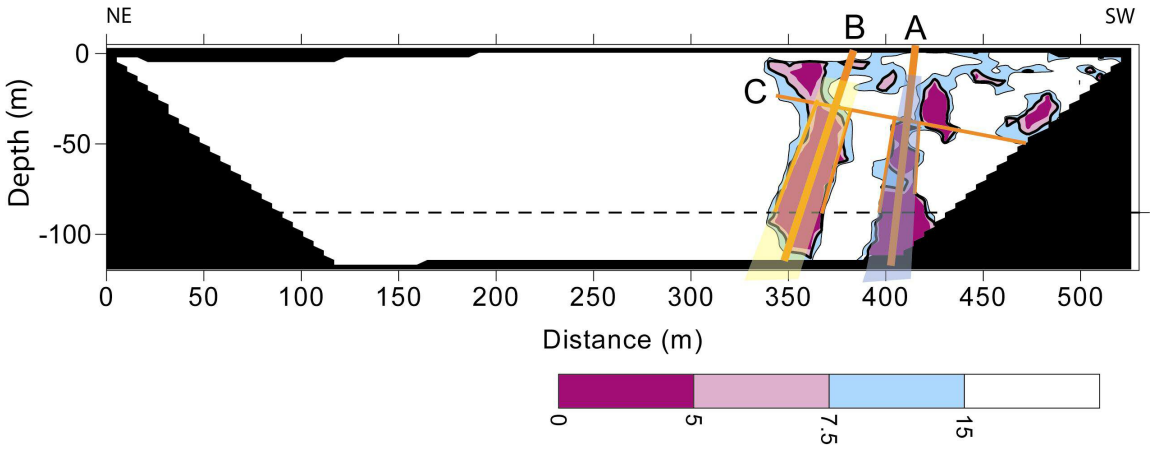

Figure 5.9. Low resistivity zone highlighted in the DH01PERP line at the Hartman Ranch site. The image shows three dipping features: A, B, and C. The shaded zones are used to represent the area used in analysis of the fault trace.

DH02N30W Analysis

The second survey conducted at the Hartman ranch was strung with the fault in the middle of the line. To the NW side of the survey are the higher resistivity West Spring Creek / Kindblade formations. At 50 and 100 meters there are two high resistivity zones that occur at around 50 meters in depth. At 150 meters there is a lower resistivity zone. There was evidence at the site that of dissolution features. At 300 meters along the line a dipping lower resistivity plane is present. This plane is dipping at 40 degrees. At 350 meters there is a vertical feature with a sharp contrast in resistivity on each side of the feature. In the Deese group, some horizontal and vertical features are evident (Figure 5.10).

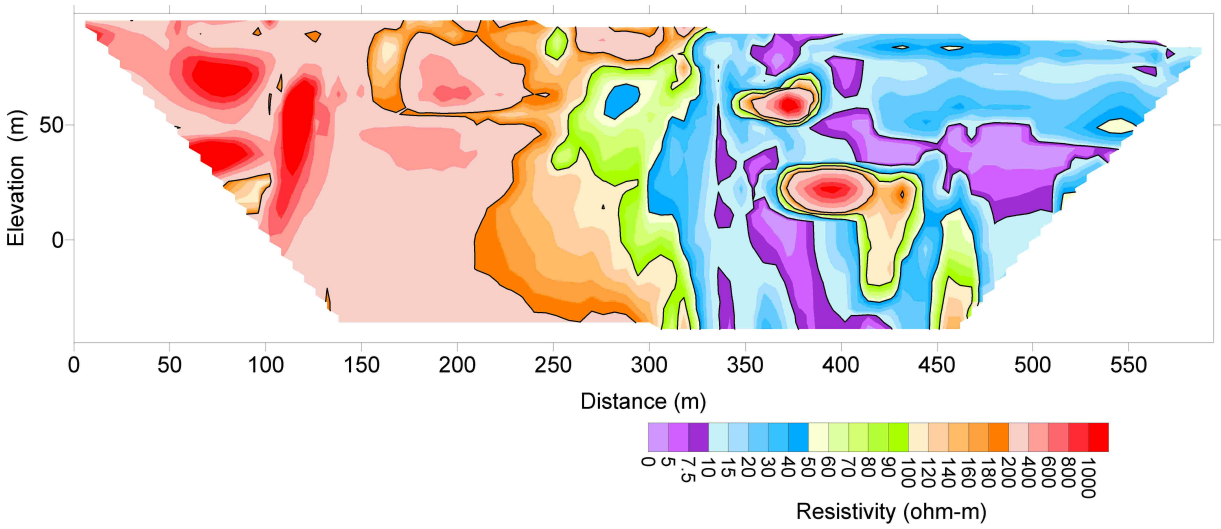

Figure 5.10. DH02N30W inverted resistivity image showing an interpreted vertical fault and a dipping bed with an apparent dip of 25 ± 5 degrees which gives a true dip of 34 degrees at 48 degrees from the fault.

Further analysis was completed on the results of this survey (Figure 5.11). Three dipping features identified. Feature A in the middle dips at 55 degrees. Feature B is a low resistivity zone with a dip of 93 degrees. Feature C is the shallowest dipping feature at 10.3 degrees.

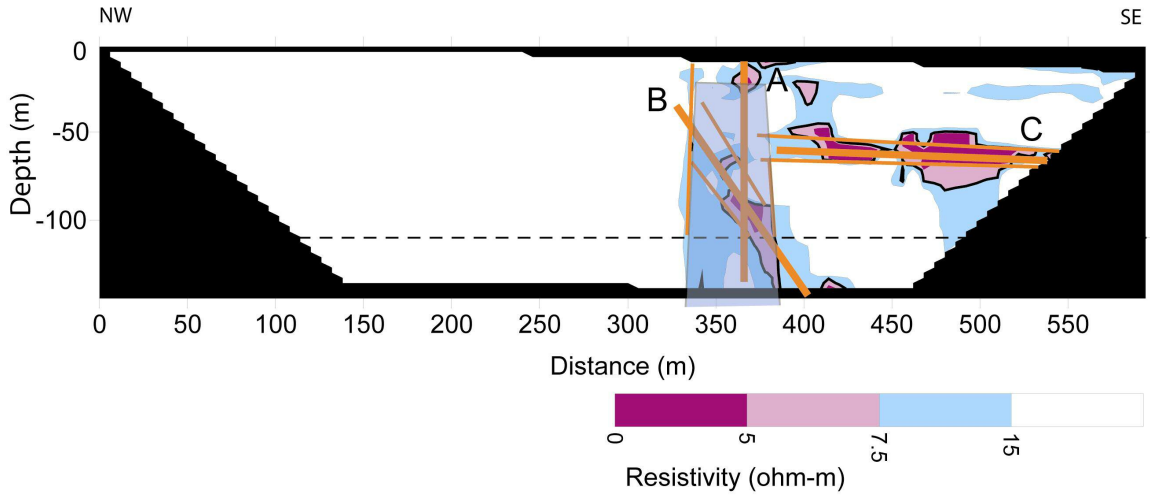

Figure 5.11. Low resistivity zone of line DH02N30W. Three dipping features were identified in the image. The shaded zone represents feature A.

DH03PARA Analysis

The third line at Hartman ranch was also the shortest. In this case only the 36 smart electrodes were used for the survey. The higher resistivity West Spring Creek and Kindblade formation is to the north – west of the 100 meter mark on this survey. There is a plane at 80 meters that dips 30 degrees to the north – west. To the south – east of the fault some low resistivity trends are evident in the Deese group as well. At 120 meters there is a slightly higher resistivity "finger" dipping at about 40 degrees (Figure 5.12).

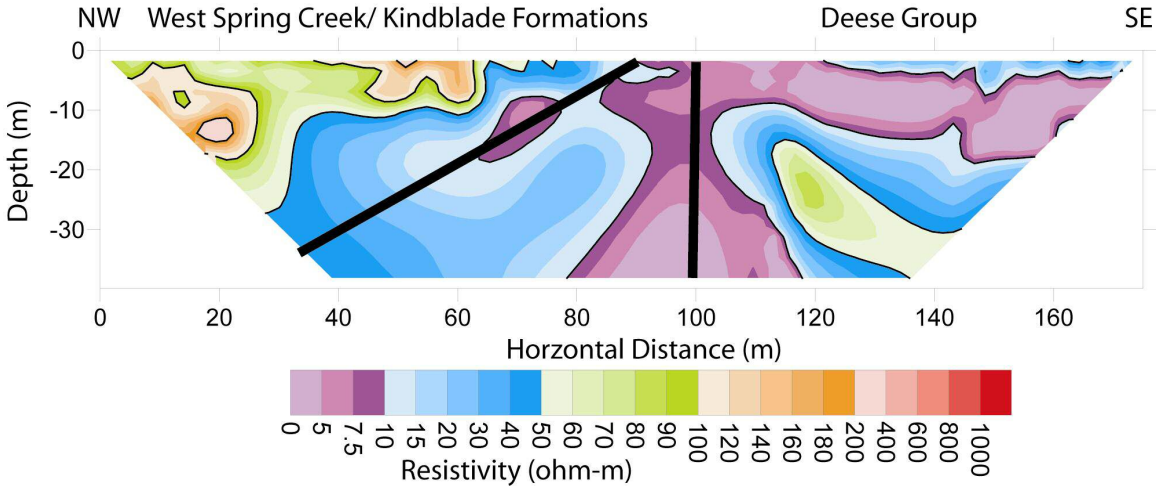

Figure 5.12. DH03PARA inverted resistivity profile showing a vertical fault and a horizontal bed dipping at 20 ± 12 degrees which gives a true dip range of 22 – 61 degrees.

Further analysis was completed on this survey (Figure 5.13). The analysis showed three dipping features in the image. Feature A which dips at 140 degrees is the middle dipping feature in the image. Feature B is the shallowest dipping feature at 10.3 degrees. Finally, feature C is the steepest dipping angle in the image with a dip of 95 degrees.

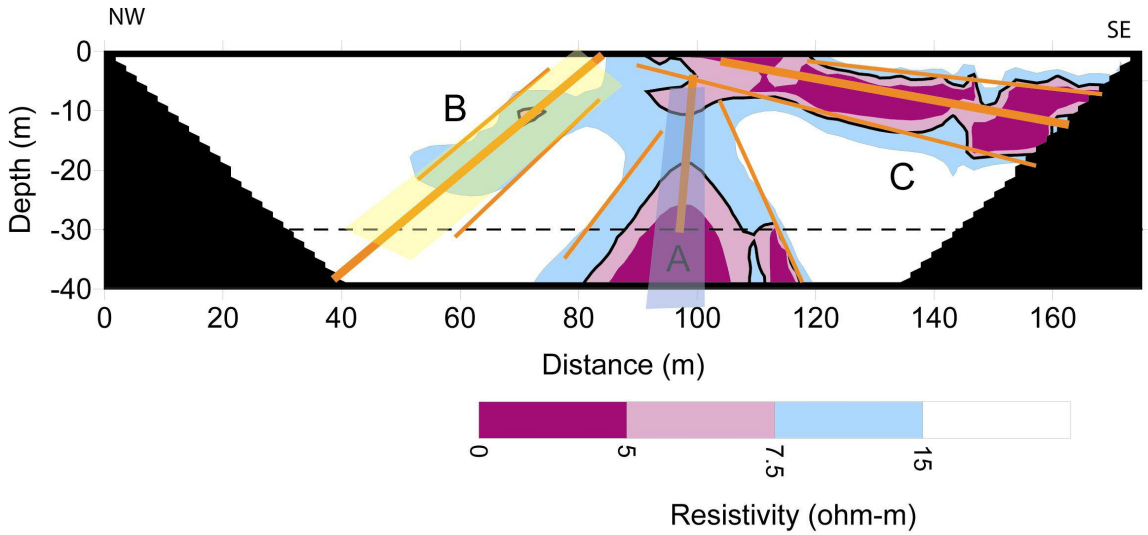

Figure 5.13. Line DH02PARA at the Hartman Ranch. Three dipping features were identified in the image. A and B are shaded in the image representing the fault zones. The spread is greater from the limited number of electrodes.

Apparent Dip of Hartman Dipping Beds

The same dipping bed can be traced through all of the surveys taken at Hartman ranch. As rotation around the fault occurs there should be a visible change in the apparent dip of the beds. For example, if a fault was dipping at 45 degrees and the survey were perpendicular to the strike, a cross-section would show the true dip. As the survey rotates closer to parallel, the dip of the fault will appear shallower and shallower. If the dip was 45 degrees and the survey was taken at 60 degrees to the fault then the apparent dip would appear to be 40.9 degrees. If the survey were rotated even further around to 30 degrees from the strike, the apparent dip drops all the way to 26.6 degrees. After 60 degrees the rate that the apparent dip changes increases dramatically. The apparent dip (A) can be calculated using the following formula:

$$(4)\ \cos Q = (\tan A)/(\tan D)$$

Where Q is the angle off of the strike and D is the true dip.

Low resistivity zone analysis reveals from survey DH01PERP, that: Feature B dips at 108 degrees and Feature C at 96 degrees. These values should be close to the true dip of these features. The apparent dips of these in DH02N30W are: Feature A is calculated at dipping 104 degrees, Feature C dips at 91 degrees. On line DH02PARA Feature A dips around 92 degrees and Feature B dips at 86 degrees.

Clement Spring Field Data

Two surveys were performed on this site. The first survey was roughly north – south, perpendicular to the fault. The second line was run at 30 degrees to the fault. The north – south survey was the longest survey completed on the site at 550 m long. The second survey was only 220 meters long due to terrain constraints.

CMT01 Analysis

CMT01 was the first line run at the Clement Springs site (Figure 5.14). To the southern end of the site are the highly resistive West Spring Creek and Kindblade Formations. East of the 150 meter mark along the line are the Oil Creek and Joins Formations. At 150 meters there is a vertical feature. This feature is represented by low resistivity, less than 50 ohm-m. There is evidence in this area that this fault is a conduit for fluid flow; discharge near the fault trace. There is a dipping feature indicated on the data from CMT01 at 200 meters, it has a resistivity of around 90 ohm-m. This feature could be a dipping bed or a conduit to water flow. A third resistivity feature is present at 400 meters. This feature has a signature that is similar to the feature at 200 meters.

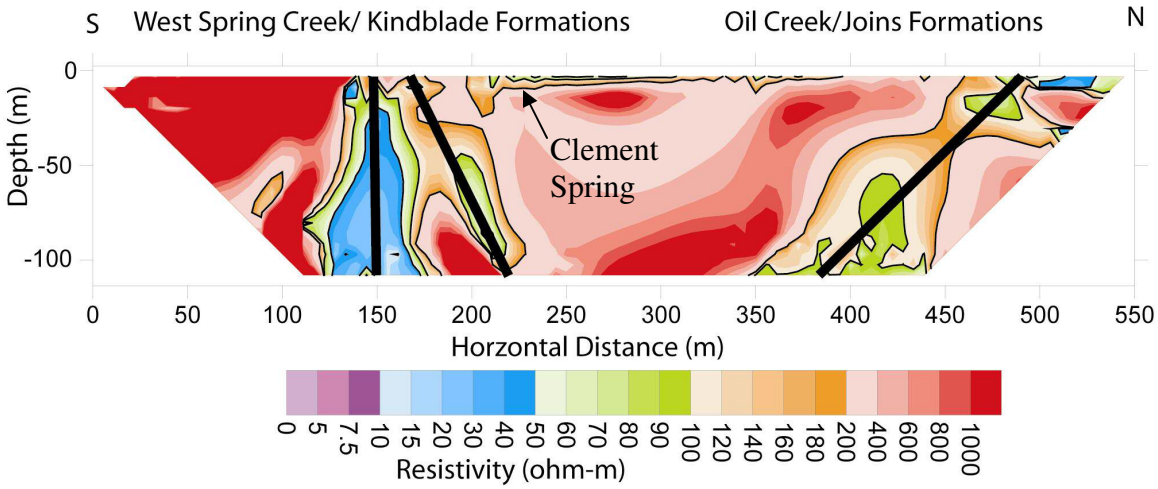

Figure 5.14. Inverted resistivity section of Clement Springs showing a fault zones. The southern fault is the South Sulphur Fault. The two other marked features are possibly conduits to fluid flow or part of faults themselves.

CMT02 Analysis

CMT02 is the second, and shortest, survey done at the Clement Springs site (Figure 5.15). This survey was oriented at 30 degrees to the strike of the fault. There were three significant features identified in this image. The first, at 110 meters, is a vertical feature with resistivity values down to 15 ohm-m. The second significant feature is the dipping low resistivity feature present at 130 meters. The third is the nearly flat feature at a depth of about 10 meters. This is a significant feature because the spring is located about 20 meters to the north of the 140 meter mark on this survey.

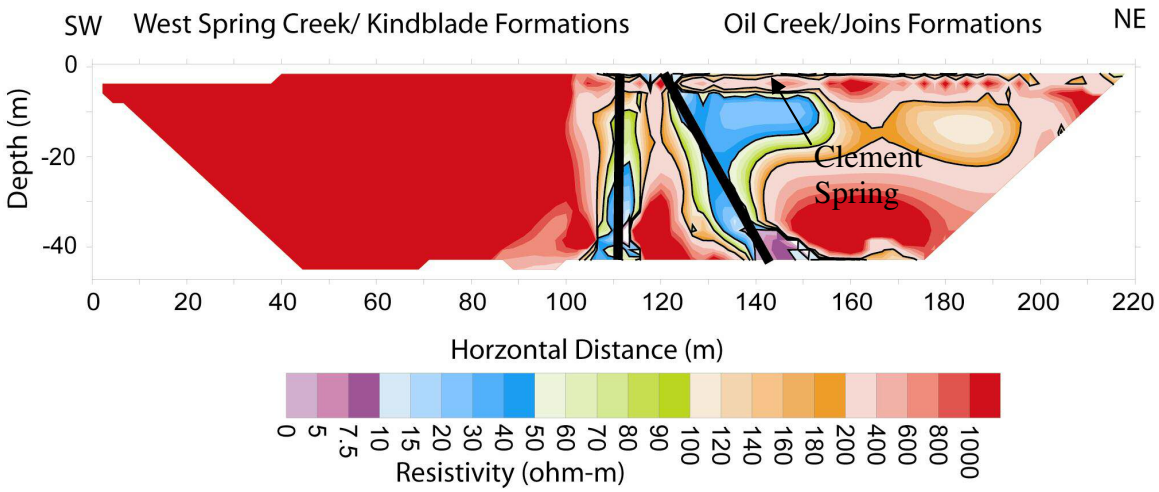

Figure 5.15. Inverted Resistivity section of Clement Spring 30 degrees to the trend of the fault. Three significant features are identified in this image. The first is interpreted as the fault located at 110 meters. The second is a fluid conduit at 130 meters. Third is a horizontal feature that may be another conduit for fluid flow, and a possible source for the spring.

Extended analysis was done on both of the Clement Spring lines (Figure 5.16).

Clement Spring Feature A is dipping at 93 degrees, Feature B is dipping at 72.4 degrees,

Feature C is dipping at 118.7 degrees and Feature D is dipping at 72.4 degrees.

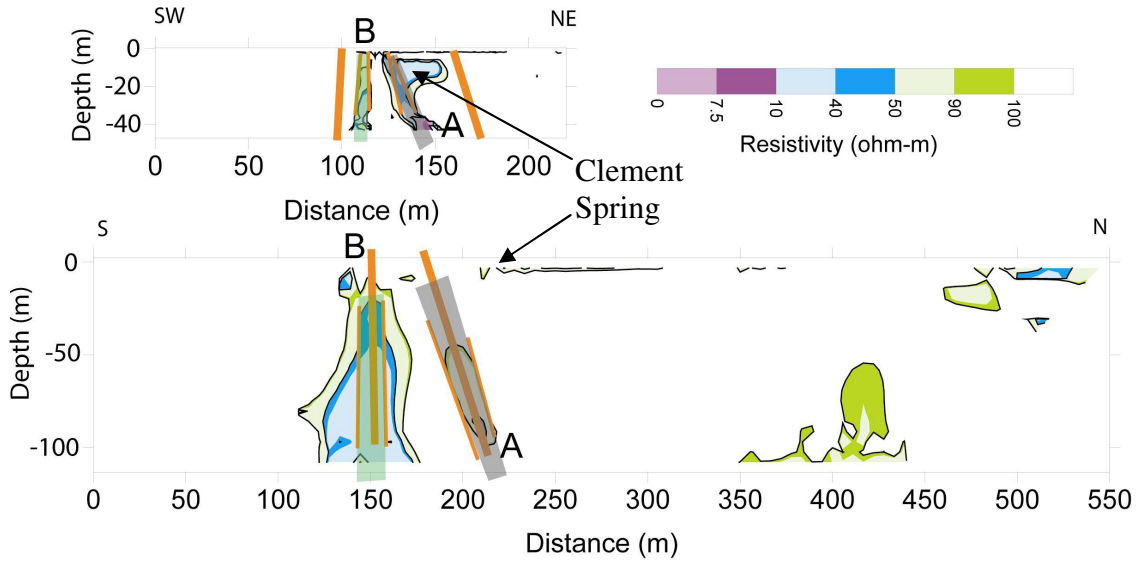

Figure 5.16. Clement Spring low resistivity analysis. Four dipping features were interpreted in the two images.

I-35 Mile Marker 49 Field Data

A single line was completed, oriented parallel to I-35 at the scenic turnout (Figure 5.17). This south to north line was 137.5 meters in length. Figure 5.17 shows the line length to be 275 meters in length. This was done to reduce the amount of relief on the image to help identify linear trends. The structural dip to the beds at this location is about 45 degrees to the north. At 125 meters along the line the first dipping feature can be seen. This feature is likely a dipping bed. In the 2x exaggerated length of the line the bed appears to dip at 30 degrees. An additional feature was identified at 150 meters and 200 meters. Unfortunately this section in the line was a low area in the terrain and did not allow for viewing the feature at the surface. However, beds do have a similar dip to the beds in the survey

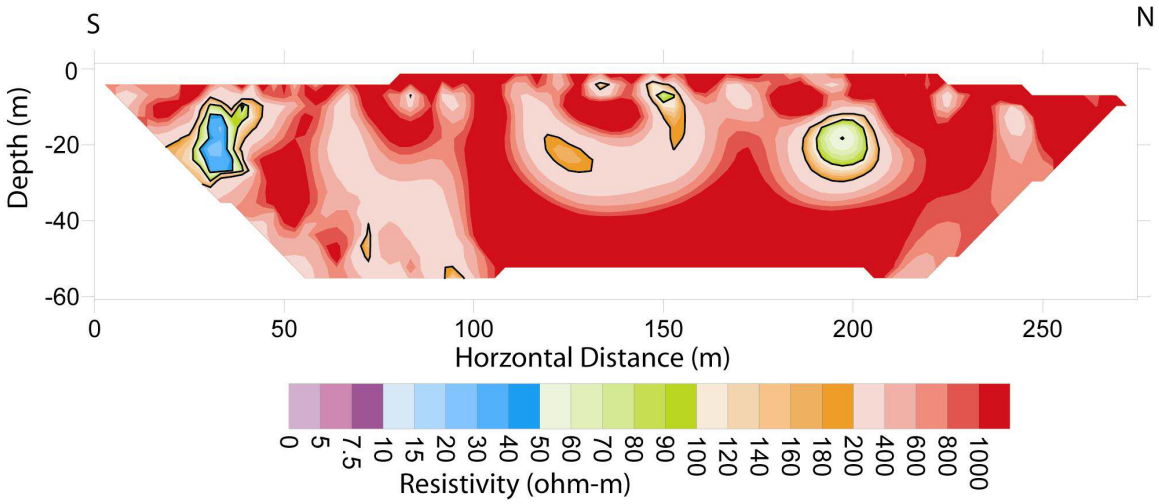

Figure 5.17. Inverted Resistivity Section showing the I-35 cross-section. Dipping beds are interpreted in the image at 125m, 150m, and 200m. A possible fault can be seen at 25m along the line.

ERI Comparison with Gravity Data

Gravity data was acquired over much of the field to identify the changes in lithology, identify changes in porosity, and locate and characterize faults and folds. The last part of these goals is the most important for this study as it contributes to identifying the faults and how they trend in the subsurface. All data collection and analysis was done by Scheirer and Scheirer (2006).

A continuous gravity survey was completed across the area (Figure 5.18). The faults that were located and identified in the surveys were the: Sulphur Fault, South Sulphur Fault, Mill Creek Fault, and Reagan Fault (Scheirer and Scheirer, 2006). The two faults that are relevant to this study are the South Sulphur Fault and the Mill Creek Fault.

The South Sulphur Fault, from the gravity modeling, shows the fault with a slight dip to the north in the western part of the study area. As the fault proceeds west the best fit in the model moves the fault more towards a vertical fault. The dipping of the fault to the north agrees with the modeled data from the resistivity for the major area of resistivity change. Figure 5.18 and 5.19 shows the gravity profile along with the resistivity line of the South Sulphur Fault.

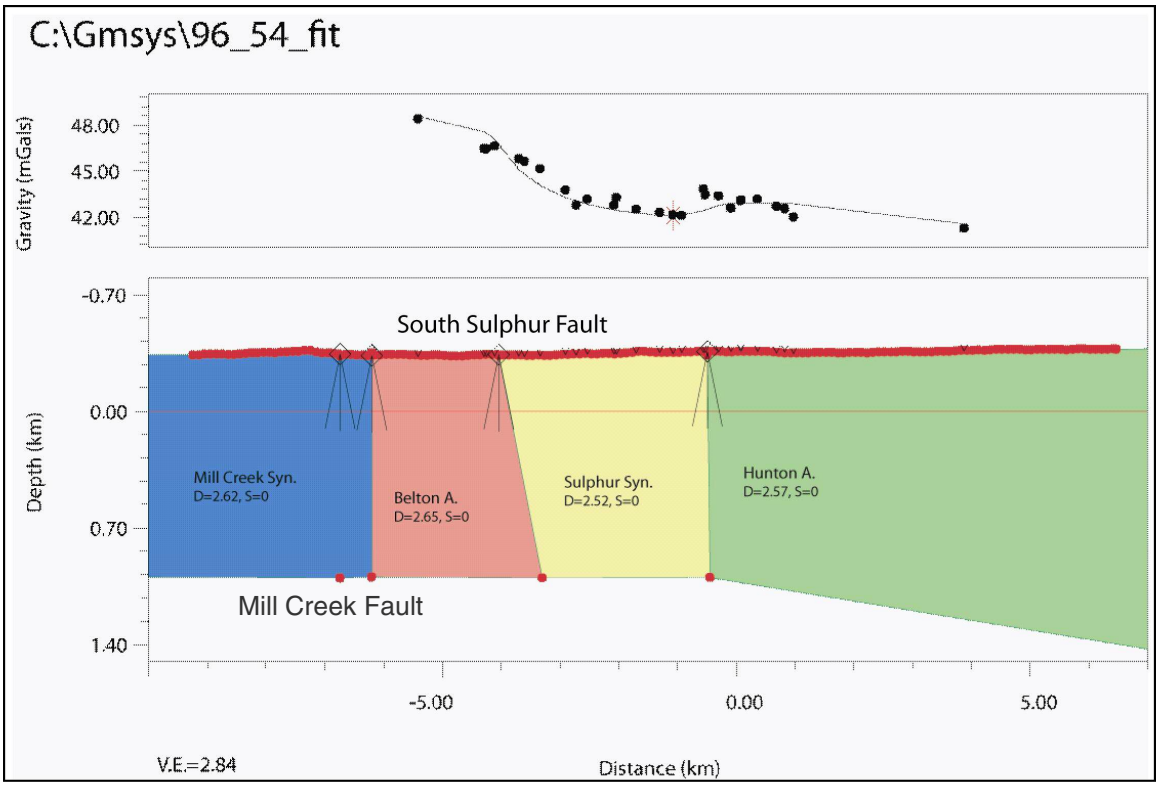

Figure 5.18. Gravity survey completed by the USGS. The South Sulphur Fault is indicated in the image as dipping to the north. The Mill Creek Fault is shown as nearly vertical (Scheirer and Scheirer, 2006).

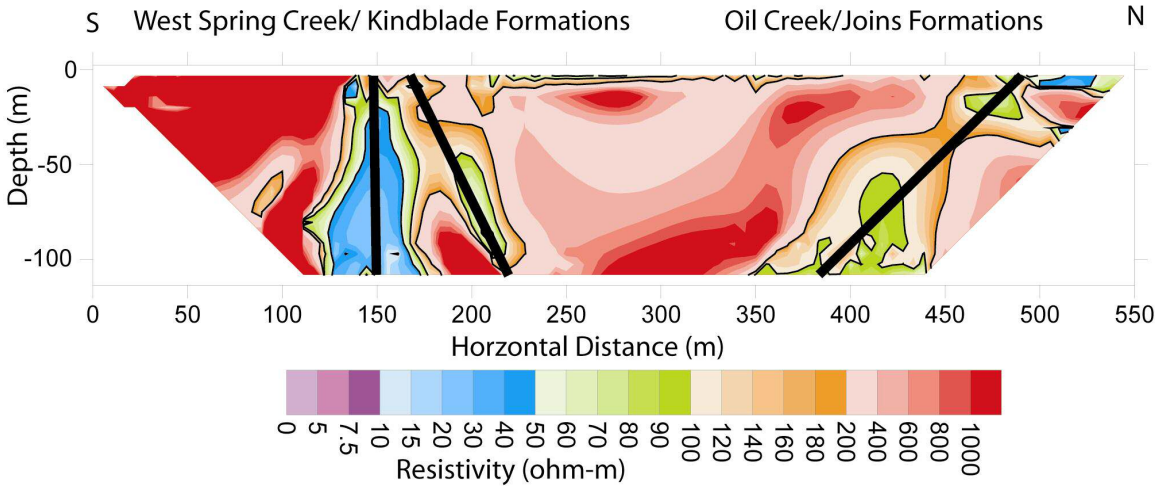

Figure 5.19. Resistivity survey of the South Sulphur Fault showing a near vertical resistivity feature at 150 meters.

The Mill Creek Fault, near Hartman Ranch, was also part of the gravity survey and shows the Mill Creek Fault at the area of the survey to be nearly vertical. This

concurs with the resistivity data that was taken at the Hartman Ranch. At the Hartman Ranch site the Mill Creek Fault seems to be a vertical fault near the surface. Figure 5.18 shows the gravity data for the area around Hartman Ranch.

CHAPTER VI

DISCUSSION

Forward modeling answered the questions on the ability to model data and addressed problems that were presented by gridded data. This work showed similar trends in the modeled data versus the field data. Field conditions that may have affected data collection are also examined.

ERI Forward Modeling

Forward modeling was completed to establish limits for the software and inversion methods. Interestingly there was a connection between the contrast ratio of the image and the ability to accurately resolve the fault. This seemed to be the result of the averaging algorithm that was used to calculate the grid values. When the contrast increased the averaging also increased in radius. This had the affect highlighting the fault and making it easier to see but the dip determination was less accurate. At lower contrasts the faults were harder to image but the dip was more accurate. From the forward modeling, it was determined that the highest error from the fault picking algorithm is at the grid corner (23 degree angle).

To obtain the best results from the forward modeling, the first and lower three points in the analysis of the fault were dropped. The field data showed similar results

with the data quality degrading with depth. Therefore the field data analysis was done with the lower three data points removed from the data set.

Grid error and depth error were always present in the data. This was an unavoidable issue that limits the resolution of faults to a minimum of about 5 degrees. An understanding of how the grid system operated helped with the picking of faults. Acquisition error was present in all data sets collected. The best way to minimize this error was by minimizing the contact resistance as much as possible. With this error reduced and the grid and depth error present, the faults could be resolved to a degree of accuracy of 5 degrees.

ERI Field Surveys

Data collection at these sites was difficult as bedrock was on or near the surface at all locations. Because of this contact resistances varied across all field sites. Salt water was added to reduce the contact resistance to below 500 ohm-m. However contact resistance affects still affected the data. Vegetation was not a factor in the placement of the surveys or had a pathway present along the length of the line.

Hartman Ranch

The Hartman Ranch had a number of sink holes on site. Sinkholes were characteristic in the dolomite and limestone along the northern half of the site. A large sinkhole was located at the north end of the preliminary line run at the site. This sinkhole was approximately 16 feet across and 15 feet deep. Overall contact resistance error was low at this site. The contact resistance for problem electrodes dropped below the upper limit of 500 ohm-m with addition of the salt water solution.

The corrected apparent dip values for low-resistivity features were used to identify two dipping beds at the Hartman Ranch field site. Feature C on line DH01PERP correlates well with Features A on DH02N30W and C on DH02PARA, which have corrected dips of approximately 90 degrees. Feature B on line DH01PERP correlates well with Feature A on line DH02PARA at around 108 degrees.

Clement Spring

The southern half of the field site is composed primarily of well indurated limestone and dolomite. This presented problems when trying to lower the contact resistance of some electrodes. Even with the salt water solution, the contact resistance for some electrodes was above the 500 ohm-m limit. This added error to the data sets; however the poorer quality data was removed to reduce the error.

A spring discharged along the fault at this site. This spring could be the source of the lower resistivity anomaly in the two images from this site. Water flowing up the fault along fractures, on bedding planes near the surface, could be the source of the water for the spring.

I-35 Mile Marker 49

This site was exposed conglomerate along the entire line. There was a large amount of drilling necessary at this site. The hole for each electrode location had to be drilled. The conglomerate was difficult to drill. The hammer drill that we were using suffered catastrophic failure approximately half way through the line. Therefore the author had to drive to town to rent a drill that could do the job.

Future Work

Future work that can be conducted is to correlate well data, magnetotellurics, and seismic to a fault that has been imaged with resistivity. Further work should be done on the algorithms used to invert the models with a focus on being able to make sharper contrasts between cells when a gradient value is over a certain threshold. Grids should be studied in further detail to examine if changing the grid shape can decrease the grid and depth errors. Deeper faults may be imaged using longer survey lines to see if the fault dip is changing with depth. Coring a fault and comparing that data to resistivity to see if porosity has an effect on the resistivity in a fault zone would be useful.

CHAPTER VII

CONCLUSIONS

Electrical resistivity imaging is a useful tool that can be used to identify fault locations and dips to an accuracy of approximately 10 degrees. Even though some sources of error are present, they are relatively minor if the following suggestions are followed:

1. Use longer lines with greater electrode density.
2. Survey as close to perpendicular to the fault as possible.
3. The closer to parallel the line is to the fault, the longer the line must be to determine the fault dip accurately.
4. Shorter line lengths induce greater error due to (1) GPS error of the end points and (2) increased grid error resulting from increased grid spacing.
5. Keep location of the fault near the center of the line.
6. The closer the fault is to the corner of the model, the greater the grid error.
7. Correct for depth error.
8. As the fault approaches vertical the depth error increases. Depth errors can be averaged to approximately 5 degrees.

For the Arbuckle-Simpson aquifer, faults are readily apparent in ERI images that extend below the water table. The faults tend to be near vertical with a fault zone width

that extends 5-10 meters. Springs in the aquifer that occur along faults may not necessary coincide with the most electrically conductive regions of an image, but do correspond to electrically conductive regions of an individual image. The fault zones tend to be uniform with depth. However, interpretation is limited to the depth that good quality data can be collected (approximately 50 – 100 meters).

BIBLIOGRAPHY

Advanced Geosciences, Inc. 2001. Instruction manual for the SuperSting R8/IP and swift pp. 1 – 50

Advanced Geosciences, Inc. 2004. Resistivity inversion software EarthImager version 1.6.8.

Cai, J., McMechan, G.A., Fisher, M.A. 1996. Application of ground-penetrating radar to investigation of near-surface fault properties in the San Francisco Bay region. Bulletin of the Seismological Society of America, v. 86, No. 5, p 1459-1470

Demanet, D., Renardy, F., Vanneste, K., Jongmans, D., Camelbeeck, T., Meghraoui, M. 2001. The use of geophysical prospecting for imaging active faults in the Roer Graben, Belgium. Geophysics, v. 66, No. 1, p 78-89

Fairchild, R.W., Hanson R. L., Davis, R. E., 1990, Hydrology of Arbuckle Mountains Area, South – Central Oklahoma, Circular 91, Norman, Oklahoma Geological Survey, p. 1-112

Griffiths, D.H., Barker, R.D. 1993. Two-dimensional resistivity imaging and modeling in areas of complex geology. Journal of Applied Geophysics. v. 29, p 211-226

Halihan, T., Paxton S., Graham, I., Fenstemaker, T., and Riley, M., 2005. Post-Remediation Evaluation of a LNAPL Site Using Electrical Resistivity Imaging, Journal of Environmental Monitoring, v 7., p. 283-287.

Ham, W.E., 1973, Regional Geology of the Arbuckle Mountains Oklahoma, in Oklahoma Geological Survey (OGS), ed., OGS Special Publication 73-3, Norman, p. 1-61.

Loke, M.H., Barker, R.D. 1996. Rapid Least-Squares Inversion of Apparent Resistivity Pseudosections by a Quasi-Newton Method. Geophysical Prospecting. v. 44, p 131-152

Louis, I.F., Raftopoulos, D., Goulis, I., Louis, I.F. 2002 Geophysical Imaging of Faults and Fault Zones in the Urban Complex of Ano Liosia Neogene Basin, Greece: Synthetic Simulation Approach and Field Investigations. International Conference on Earth Sciences and Electronics, Oct. 2002. p 269-285

Nguyen, F., Garambois, S., Jongmans, D., Pirard, E., Loke, M.H. 2005 Image processing of 2D resistivity data for imaging faults. Journal of Applied Geophysics, V. 57, p 260-277

Ramirez, A.L., Daily, W., LaBrecque, D., Owen, E. and Chesnut, D. 1993. Monitoring an underground steam injection process using electrical resistivity tomography. Water Resources Research, v. 29, p 73-87.

"Resistance." Merriam-Webster Online Dictionary. 2004. http://www.merriam-webster.com (2 Jan. 2004).

Reynolds, J. M. 1997. An Introduction to Applied and Environmental Geophysics. John Wiley & Sons, Chichester, England.

Scheirer, D.S., Scheirer, A.H. 2006 Gravity Investigations of the Chickasaw National Recreation Area, south-central Oklahoma. United States Geological Survey, Open-file report 2006-1083

Suzuki, K., Toda, S., Kusunoki, K., Fujimitsu, Y., Mogi, T., Jomori, A. 2000. Case studies of electrical and electromagnetic methods applied to mapping active faults beneath the thick quaternary. Engineering Geology, v. 56, p 29-45

VITA

Mathew Ellis Riley

Candidate for the Degree of

Master of Science

Thesis: INVESTIGATION OF FAULT PROPERTIES USING ELECTRICAL RESISTIVITY

Major Field: Geology

Biographical:

Personal Data: Born in Oklahoma City, Oklahoma, On June 10, 1981, the son of Richard and Anne Riley.

Education: Graduated from Western Heights High School, Oklahoma City, Oklahoma in May 1999; received Bachelor of Science degree in Geology from Oklahoma State University, Stillwater, Oklahoma in August 2004. Completed the requirements for the Master of Science degree with a major in Geology at Oklahoma State University in May, 2007

Experience: Raised in a house in Oklahoma City, Oklahoma; employed by Garden Ridge as a customer service representative; employed by Oklahoma State University, Department of Geology as an undergraduate and graduate research assistant; Oklahoma State University, Department of Geology, 2001 – May 2006; employed by Dominion Exploration and Production as an associate geologist; July 2006 – present.

Professional Memberships: Geological Society of America, American Association of Petroleum Geologists, Rocky Mountain Association of Geologists, Oklahoma City Geological Society, Rocky Mountain Section – Society of Economic Paleontologists and Mineralogists

Name: Mathew Riley Date of Degree: May, 2007

Institution: Oklahoma State University Location: Stillwater, Oklahoma

Title of Study: INVESTIGATION OF FAULT PROPERTIES USING ELECTRICAL RESISTIVITY

Pages in Study: 56 Candidate for the Degree of Master of Science

Major Field: Geology

Scope and Method of Study: Forward modeling of Electrical Resistivity Imaging was performed to define the limits present in the algorithms and grids. An analysis was completed of these limits by forward modeling 44 models with the Halihan-Fenstemaker method of acquisition and processing. Twenty four forward models were also run with other arrays and standard processing techniques. Field data was acquired at three field sites in the Arbuckle-Simpson study area. The first site was a saturated fault without water flow at the surface. The second site was a saturated fault with spring flow at the surface. The third site was an unsaturated fault, exposed, and had no water flow. These were examined to determine if resistivity can identify faults that are conduits to flow or barriers to flow.

Findings and Conclusions: Electrical Resistivity Imaging is a viable technique to use for locating and identifying fault properties. Error is present in the method but can be minimized. There are three types of errors present from the numerical modeling of ERI data: grid error, depth error, and inversion error. Grid error is the result of the shape of the rectangular grid. This does not allow precise calculations for straight lines that are at an angle to the grid. Inversion error is the result of the grid values being calculated on the nodes of the grid and data being present in the grid center. Contrast error is a result of the averaging algorithm. As the contrast between two objects increases the averaging algorithm causing broadening of the contrast front further from the contact of the two resistivities. This has the effect of making the fault more apparent in the image but lowers the precision the fault location can be selected. Once these are understood more informed analysis can be performed on inverted images. This is shown in the field studies done in the Arbuckle-Simpson Aquifer study. Resistivity can be used to determine if a fault is saturated or unsaturated, and may be able to infer if the fault is hydraulically conductive.

Advisor's Approval: Dr. Todd Halihan